
Control of a Photovoltaic-Electrolysis System

- P4 Report -

Project Report
AIE4-E23

Aalborg University
AAU Energy

Copyright © Aalborg University 2023

L^AT_EX used for formatting.



AALBORG UNIVERSITY
STUDENT REPORT

Energy Department
Aalborg University
<http://www.aau.dk>

Title:
Control of a
Photovoltaic-Electrolysis System

Theme:
Control Systems

Project Period:
Spring Semester 2023

Project Group:
AIE4-E23

Participant(s):
Dawid Marusarz
Edgar Vivas Jover-Santina
Miguel Ángel García Otalora
Nils Albin Emil Nolemo
Visnu Ritesh Vijayakumaar Palanisamy

Supervisor(s):
Amin Hajizadeh

Copies: 1

Page Numbers: 72

Date of Completion:
May 25, 2023

Abstract:

The report aims to provide an optimised system to implement the conversion of solar energy to hydrogen as a response to the growing interest of combining Power-to-X and renewable technologies. The presented system utilises a DC-DC boost converter to change the voltage levels provided to an electrolyser.

Linear models of a PV panel, DC-DC boost converter, and the electrolyser are presented in the report. The model of the DC-DC boost converter is studied from a control theory perspective to understand the behaviour of the model so that the output voltage of the DC-DC converter can be controlled effectively. Some of the available tools used to study a linear time-invariant system are used to study the linear model of the converter.

Two distinct modes of operation are presented in the report: Maximum Power Point Tracking (MPPT) and Proportional-Integral (PI) control. The MPPT mode calculates the duty cycle necessary for the output voltage to be in Maximum Power Point (MPP), whereas the PI controller calculates the duty cycle for the output voltage to the electrolyser to be stable at a setpoint. The electrolyser, therefore, operates in a voltage-controlled mode. Empirical data obtained from testing the proof-of-concept system are displayed and discussed in the report to validate the design of the models and controllers.

The content of this report is freely available, but publication (with reference) may only be pursued due to agreement with the author.

Contents

Preface	v
Nomenclature	vii
1 Introduction	1
2 Problem Analysis	2
2.1 Power-to-X	2
2.2 Electrolysis	3
2.2.1 Electrolyser Types	4
2.3 Photovoltaic Technology	6
2.3.1 Maximum Power Point Tracking	6
2.3.2 MPPT Algorithms for Photovoltaic Cells	7
2.4 DC-DC Conversion	9
2.5 Problem Delimitation	14
2.5.1 Electrolyser Choice	14
2.5.2 MPPT Algorithm Choice	15
2.5.3 DC-DC Converter Choice	15
3 Problem Solution	16
3.1 Modelling	16

3.1.1	Alkaline Electrolyser	16
3.1.2	PV Cell and MPPT Algorithm	19
3.1.3	Modelling and Control of Boost Converter	23
3.1.4	Control	35
3.2	Simulation	38
3.2.1	Simulation of DC-DC Boost Converter Model with Controller	38
3.2.2	Simulation of PV and MPPT Models	41
3.2.3	Integrated Model	44
4	Testing and Validation	46
4.1	Implementation	46
4.1.1	Microcontroller	47
4.1.2	Sensors	47
4.1.3	Boost Converter	49
4.1.4	Panel	49
4.2	Experiments	50
4.2.1	PI Controller with a Power Supply	50
4.2.2	MPPT and PI Controllers with a PV Panel	53
4.2.3	MPPT accuracy	56
5	Discussion and Conclusion	59
5.1	Discussion	59
5.2	Conclusion	60
Bibliography		61
A Final Arduino Script for the Integrated System		66
B Final MATLAB Script for the MPPT		71

Preface

This report was done by a fourth semester group of the Applied Industrial Electronics program at Aalborg University in Esbjerg. The project was completed as part of fulfilling the curriculum for the project course in **Control Systems**. The topic was inspired by the growing focus on Power-to-X research at the university and in industry across Denmark and globally.

Aalborg University, May 25, 2023



Nils Albin Emil Nolemo
<nnolem21@student.aau.dk>



Edgar Vivas
<evivas21@student.aau.dk>



Dawid Marusarz
<dmarus21@student.aau.dk>



Miguel Angel Garcia Otalora
<maga21@student.aau.dk>



Visnu Ritesh Vijayakumaar Palanisamy
<vrvi21@student.aau.dk>

Nomenclature

Acronym	Definition
PtX	Power-to-X
PV	Photovoltaic
MPP	Maximum Power Point
MPPT	Maximum Power Point Tracking
PEM	Proton-Exchange Membrane
P&O	Perturb and Observe
INC	Incremental Conductance
FOCV	Fractional Open Circuit Voltage
MOSFET	Metal Oxide Semiconductor Field Effect Transistor
BJT	Bipolar Junction Transistor
IGBT	Insulated-Gate Bipolar Transistor
PWM	Pulse Width Modulation
ADC	Analog-to-Digital Converter
CMRR	Common-Mode Rejection Ratio
PID	Proportional-Intgeral-Derivative
PI	Proportional-Integral

Chapter 1

Introduction

Power-to-X technology is where one form of energy is converted to other forms of usable energy. This conversion allows for using excess energy in fields other than direct energy consumption. The form of energy can differ depending on the use case. Several compounds commonly observed in practical applications include hydrogen, methane, ammonia, and diesel. These forms of energy can then be used in other sectors such as transport and aviation while also de-carbonizing these industries. It is a flexible means of long-term storage and distribution for renewable energy [1] [2]. Because of this, the Danish government has formulated an official strategy regarding PtX with objectives covering climate, legislation, integration, and technology aspects [3].

The ability to integrate and coordinate several sectors, including the transportation and electrical sectors, is a significant benefit of Power to X technology. The innovation can produce a more responsive energy system that can adapt to shifts in supply and demand. This is crucial for renewable energy sources, which are frequently unpredictable and sporadic in their energy production [4]. By employing PtX to transform surplus renewable energy into fuels that can be stored and transported, the reliance on conventional energy sources can be reduced and more sustainable energy systems can be developed [1]. PtX technology has the potential to significantly alter the global energy environment and aid in the achievement of climate goals.

Given the move towards a larger and growing share of renewable energies in the energy mix, research and development tied to utilizing this energy in its totality will become an increasingly important pursuit, thus an initiating question for further inquiry into this field is defined as follows:

Can renewable energy be utilized efficiently for PtX applications, and can this be improved to become economically beneficial?

Chapter 2

Problem Analysis

2.1 Power-to-X

In May of 2022 the European Commission presented RePowerEU, a strategy and funding initiative for the European energy sector to end its dependence on natural gas imports [5]. This implemented further goals of expanding renewable energy technologies in the European Union (EU), among other goals setting the target of a 45% renewable energy mix by 2030. With increasing intermittent energy sources such as wind and solar, issues with the variable energy generation and energy demand patterns are likely to become an increasing problem as these sources represent a larger part of the energy mix. The issue is not always the lack of power generation, but can also suffer from overproduction, meaning that sources must be temporarily disconnected to maintain grid stability, called curtailment. This loss of energy is something which could possibly be utilized for energy storage, lowering the amount of wasted energy [6].

Excess energy could be stored for direct use at times when production falls below demand but could also be used in the effort to lower emissions in sectors where direct electrification is not viable. Direct electrification is a term referring to direct replacement of fuel sources with electric ones [7]. The Danish government published a document in 2020 laying out its official strategy regarding Power-to-X, framing what goals it has with funding and developing this PtX technologies. The main goals that are laid out in this strategy is to produce hydrogen and bio-fuels to transition heavy transport like airplanes and shipping to run on carbon neutrally produced fuels from PtX processes, mainly hydrogen and derivatives thereof [3]. The increasing focus on hydrogen is not merely for its future potential as a part of a solution to increasing energy demands, but also as an investment in decarbonising current hydrogen production. As of 2018 an estimated 70 million tonnes of pure hydrogen was produced globally per year and growing. This was mainly produced

using natural gas and coal, accounting for about 6% of global natural gas use and 2% of coal, leading to emissions of an estimated 830Mt of CO₂ per year [8]. The source used to produce hydrogen is categorised using colours as follows [9]:

- **Black and Brown:** Production using black or brown coal.
- **Blue and Grey:** Production using natural gas. The difference being that blue incorporates carbon capture in the process to reduce emissions, while grey does not.
- **Pink:** Production using nuclear sources.
- **Green:** Utilizing renewable energy sources.

In order to accelerate the transition to hydrogen being a larger and more diversified part of the energy mix, the Danish government has set up a number of funding schemes to promote it. As outlined in the Danish PtX strategy document, 1.25 billion DKK have been earmarked for production support of hydrogen and other PtX products over a ten-year period. Additionally, investment plans of 344 million DKK towards hydrogen and PtX ventures have been made in cooperation with the REACT-EU initiative and Just Transition Fund [3]. As a result, there are some 20 different commercial PtX projects planned in Denmark as of 2020. These comprise mainly of hydrogen production, some for direct use and some for further processing into methanol and ammonia. Two of these projects are planned to be built in Esbjerg, one aimed for hydrogen and one for ammonia. These will have a production capacity of up to 1 GW, making them both potentially the largest in Europe [10].

Given the increasing interest in PtX technologies from the European Union, the Danish government, and the private sector, in particular regarding hydrogen production, it seems a worthwhile area to explore and research further to find out if it can be made an economically competitive energy storage source using renewable sources. Though it is possible to investigate this for different sources, wind, solar, nuclear and the like, in this project it has been limited to solar, as solar energy PtX is a sparsely researched area.

2.2 Electrolysis

Electrolysis is a process that uses direct electric current to produce hydrogen. It is a widely used process to separate a substance into its original elements. The first documented electrolysis experiment was conducted in 1789 using electrostatic current generated by friction [11] [12]. In 1800, with the help of the newly invented voltaic pile, near-constant current was used to split water into two volumes of hydrogen and one volume of oxygen [13]. By the end of 19th century, industrial methods for electrolysis were developed [14]. In spite

of these advancements, electric decomposition of water did not become a widespread process during the Industrial Revolution. Fossil fuels (coal, oil, and gas) became a cheaper and more efficient alternative for both off-grid energy storage and hydrogen and oxygen production. In the 20th century electrolysis played an important role in several industrial processes, such as producing aluminium, chlorine, and sodium hydroxide, as well as improving certain properties of metals with electroplating and anodizing.

In the 21st century electrolysis is meant to play a key role in the energy landscape. As renewable energies grow in production and both national and supranational strategies seek to phase out fossil fuels, there is a need for a carbon-free generation of hydrogen. This combined with further advancements in electrolyser technologies has created an opportunity for off-grid renewable installations that use hydrogen as a backup, as opposed to diesel generators [15].

2.2.1 Electrolyser Types

There are three types of electrolyzers based on their electrolyte types. These are: Alkaline, Proton-Exchange Membrane (PEM), and Solid Oxide.

- Alkaline electrolyzers were the first ones used and they typically use a porous diaphragm between the anode and the cathode and a liquid alkaline electrolyte (a solution with KOH or NaOH). Since the electrocatalyst is diluted in this caustic water solution, the raw materials required for its construction are readily available ones, such as asbestos for the membrane and nickel-treated steel for the electrodes [16]. A typical, modern configuration for an alkaline electrolyser is the bipolar one, where several isolated electrolyzers are connected in series or parallel to achieve the desired current and voltage characteristics [17].
- PEM electrolyzers have a similar structure to the alkaline counterparts. They differ on the materials used and how they are put together. There is a membrane electrode assembly which consist of very thin electrodes and membrane, in the range of the micrometres [18]. Electrodes are usually made of carbon cloth or carbon fibre papers embedded with noble metals, while the membrane is made of Nafion, which is a brand name for perfluorosulfonic acid. The membrane is a polymer electrolyte; therefore, the electrolyser works just with water, and there is no voltage drop in the liquid, which makes PEM technology highly efficient. The downside, together with the sourcing of materials is that the membrane becomes strongly acidic after being soaked in water, which affects longevity and maintenance of the device [19].
- Solid Oxide electrolyzers use a solid electrolyte, typically a layer of yttria-stabilized zirconia. It is also characterized for using porous electrodes, a fuel electrode for the cathode and an oxygen electrode anode [20]. The assembly operates as a fuel cell

running in reverse mode, also called regenerative mode. The operating temperatures are over 800°C and offer high efficiency for large scale setups [21].

Table 2.1: Characteristics of alkaline, PEM, and Solid Oxide electrolyzers [22]

	Alkaline	PEM	Solid Oxide
Development stage	Commercial	Commercial	Research and development
Electrolyte	Aquous alkaline (KPH or NaOH)	Solid polymer membrane (Nafion)	ZrO ₂ ceramic doped with Y ₂ O
H ₂ production (m ³ /h)	<760	<450	
MW equivalency	≈2.7	≈1.6	
Charge carrier	OH ⁻	H ₃ O ⁺ / H ⁺	O ²
Cell temperature (°C)	40-90	20-100	800-1000
Cell voltage (V)	1.8-2.4	1.8-2.2	0.91-1.3
Cold start time	Minutes-hours	Seconds-minutes	-
Advantages	Available for large plant sizes, cost, lifetime	No corrosive substances, high power densities, high pressure > 100 bar, dynamics	High electrical efficiency, integration of waste heat possible
Disadvantages	Low current density, maintenance costs (system is highly corrosive)	Expensive, fast degradation	Limited long-term stability of the cells, not suited to fluctuating systems, expensive
Transient operation	Possible, but leads to problems; reduction up to 20% load possible; over-load operation possible	Better than AEL, dynamic adjustment possible, partial (down to 5%) and overload operation possible	Not well suited
Renovations/ life-time	Renovations: 8-12 years; Lifetime: up to 30 years	Lifetime: 5 years	

The three introduced electrolyser types have applications and scenarios where they are the most suitable choice, depending on a range of factors: such as location, economics, maintenance, ambient temperature, or space available. It should be noted that for any of them, when connected to renewables and due to intermittence, it is important to control the amount of power delivered to the unit. This can be achieved by using different algorithms and converters, which will help ensure a proper production and guarantee the longevity of the device.

2.3 Photovoltaic Technology

Solar energy is one of the renewable energy forms set to produce a large portion of the world's energy in the future. According to an IEA report it saw the largest growth in installed capacity among renewables between 2019 and 2021 [23]. Given its growth it is likely to be a part of future PtX systems. It will thus be important and necessary to make sure that the panels are utilised to their fullest.

2.3.1 Maximum Power Point Tracking

Maximum Power Point Tracking (MPPT) is commonly used to improve power delivery from photovoltaic cells. It ensures continuous work on the maximum power point which is illustrated on the current-voltage curve of a solar panel seen in figure 2.1.

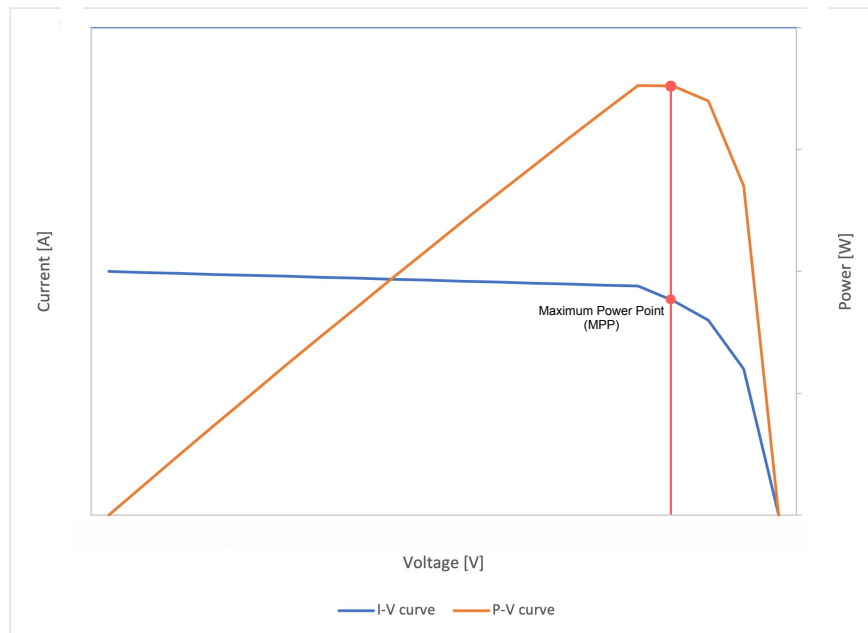


Figure 2.1: Correlation between I-V and P-V graphs [24].

By multiplying current and voltage the power output of the PV cell is obtained. An MPPT algorithm constantly checks the output value and ensures the system works with the highest possible power output.

2.3.2 MPPT Algorithms for Photovoltaic Cells

By monitoring the maximum power point of the PV module, which varies based on operational variables including temperature, solar irradiation, and load, an MPPT algorithm is able to maximize the power output of a PV system. There are many available and widely used algorithms to track maximum power points. The most used one is the Perturb and Observe algorithm because of its simplicity [25]. There are, however, many more algorithms that can be implemented in order to improve the overall efficiency of the system. They offer different approaches to obtain maximum power points and differ in complexity. Some of the vital MPPT algorithms that could be used in this project are discussed in this section.

Perturb and Observe

Perturb and Observe is a simple and widely used algorithm. The P&O algorithm idea is to alter the PV module's operational point and track any changes in power output that occur. The algorithm then compares the power output at the current operating point with the previous one. If it increases, the algorithm continues to move in the same direction, if not, it perturbs in the opposite direction until the Maximum Power Point is reached [26].

The P&O algorithm's ease of use and relatively low demands compared to other algorithms are the main benefits of implementing this algorithm. Furthermore, under steady-state conditions, it tracks the MPP accurately. However, the P&O algorithm does not produce reliable results when it comes to dynamic and constantly changing environmental conditions. It can get stuck at a local maximum and therefore does not give the proper MPP. Moreover, the P&O algorithm can lead to oscillations at the MPP, which could lower the total efficiency of the PV system [27].

Incremental Conductance

Incremental Conductance is another MPPT algorithm that is widely used in PV systems. The algorithm compares the PV module's incremental conductance and its instantaneous conductance. The incremental conductance is the change in power output with respect to the change in voltage, whereas the instantaneous conductance is the derivative of the power-voltage curve at the current operating point. The Incremental Conductance algorithm modifies the PV module's operating point so that the incremental conductance is zero, which is equivalent to the maximum power point [26].

Compared to the P&O method, the INC algorithm has a few advantages. Firstly, both in steady-state and dynamic situations, it can precisely track the MPP. Secondly, compared

to the P&O method, it is less prone to become stuck in local maxima. Thirdly, it can reduce oscillations around the MPP, which can boost the PV systems overall effectiveness. The INC technique is however more intricate and computationally intensive than the P&O algorithm [28].

Hill Climbing

The Hill Climbing algorithm is an advanced Maximum Power Point Tracking (MPPT) technique used in photovoltaic (PV) systems. It continuously adjusts the operating point of the PV modules to maximize the instantaneous power output. By iteratively comparing the power output at the current operating point with nearby points, the algorithm incrementally adjusts the voltage or current in the direction that increases power. This adjustment process continues until no further increase in power is observed, indicating the maximum power point (MPP) has been reached.

Compared to other MPPT methods like the Perturb and Observe (PO) algorithm, the Hill Climbing algorithm exhibits distinct behaviour. It is less prone to getting stuck in local maxima, allowing it to more accurately identify and maintain the true MPP, even under changing environmental conditions. Additionally, the Hill Climbing algorithm reduces oscillations around the MPP, resulting in a more stable and efficient operation of the PV system. However, it is important to note that the Hill Climbing algorithm requires more computational resources compared to simpler MPPT techniques. This increased computational intensity stems from the continuous evaluation and adjustment of the operating point, especially in larger-scale PV systems. Nevertheless, the precise MPP tracking, reduced oscillations, and improved system stability make the Hill Climbing algorithm an effective choice for maximising PV system performance.[29] [30].

Fractional Open Circuit Voltage

The Fractional Open Circuit Voltage (FOCV) algorithm is a widely employed Maximum Power Point Tracking (MPPT) technique in photovoltaic (PV) systems. This algorithm estimates the maximum power point (MPP) voltage by periodically measuring the open circuit voltage of the PV array and adjusting the voltage reference using a fractional multiplier. By continuously modifying the multiplier based on the relationship between the measured open circuit voltage and the estimated MPP voltage, the FOCV algorithm accurately tracks the MPP, enabling optimal power extraction from the PV system. It offers reliable performance in varying environmental conditions and has relatively lower computational complexity compared to other sophisticated MPPT techniques.

The FOCV algorithm's effectiveness lies in its ability to precisely track the MPP while maintaining operational efficiency. By leveraging periodic open circuit voltage measure-

ments and a fractional voltage multiplier, it ensures that the PV system operates at its maximum power point, maximizing power output. [31].

2.4 DC-DC Conversion

To facilitate synchronisation between the PV system and the electrolyser system, an intermediary medium is necessary. The output of the PV system can be plotted on a P-V graph, and an MPPT algorithm can be utilized to determine the maximum power output. Once the optimal voltage is determined, the MPPT algorithm can regulate the output to generate the ideal voltage and current that match the algorithms findings. At this point, a power converter is required to provide a stable and appropriate voltage to the electrolyser. The PV and electrolyser systems function at different voltage levels, and thus must be connected through the converter. It is necessary to identify appropriate models that can regulate the electrolyzers power output. This section provides an overview of commonly employed DC-DC converters, which is necessary knowledge to connect the two essential components of the system - the PV module (including the MPPT) and the electrolyser.

There are two primary types of DC-DC converters: the linear DC-DC converter and the switching DC-DC converter. The linear DC-DC converter is simple to implement and does not require complex circuitry. A basic form of a linear converter is the voltage divider, which is used to step down voltage. The power difference between the input and output is dissipated as heat, which can lead to overheating if the voltage difference is significant. Linear converters are often utilized in applications that are affected by electromagnetic interference and require high-quality voltage output with low voltage ripple. These converters are commonly seen in low-power devices, but are generally not preferred due to their low efficiency, which typically ranges from 60% to 70% [32].

Compared to the linear DC-DC converter, the switching DC-DC converter is commonly preferred due to its higher efficiency and lack of overheating problems. A switching DC-DC converter employs a capacitor that stores energy when electric pulses are given as input. The use of a capacitor allows for a smoother output voltage signal to be supplied to the connected load. The switching mechanism involved in a DC-DC converter typically utilizes a MOSFET, BJT, or IGBT. The switching component is an essential aspect of the DC-DC converter, and it is activated by a Pulse Width Modulation (PWM) signal. The typical efficiency of switching converters range from 85% to 90%. The switching DC-DC converter model can be modified to obtain different results. The three types of switching DC-DC converters are Buck converter or step-down converter, boost converter or step-up converter and buck-boost converter or universal DC-DC converter [32].

DC-DC Buck Converter

A buck converter is a type of DC-DC converter that reduces one voltage level to a lower voltage level. In contrast to linear converters, the buck converter employs components such as an inductor, capacitor, and switching element to regulate the output voltage and maintain a steady state [33].

The buck converter operates in two modes when it converts a higher voltage level to a lower voltage level: ON mode and OFF mode. In the ON mode, the switch used in the converter is closed, and in the OFF mode, the switch is open. The duty cycle ratio is the ratio between period for which the switch is in the ON mode over the total time taken for one cycle [33].

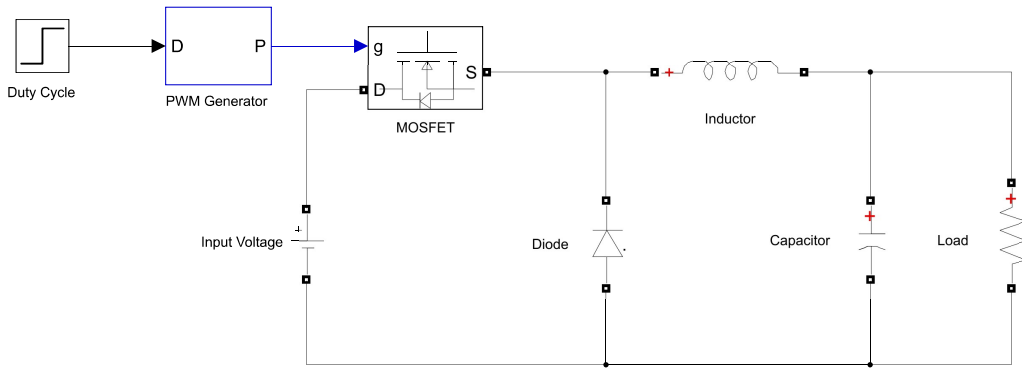


Figure 2.2: DC-DC Buck Converter.

During the ON mode of the buck converter the switch is closed, and current flows through the inductor. This current is equal to the total current flowing through the circuit. The current in the inductor is equal to the sum of the current flowing through the capacitor and the load: $I_L = I_C + I_R$ where I_L is the current across the inductor, I_C is the current across the capacitor and I_R is the current across the resistive load. The voltage across the inductor is equal to the voltage difference between the input voltage and the output voltage seen in the resistive load. The ripple current flowing through the inductor can be calculated using the voltage and current relationship for an inductor. Using this relationship, an equation can be derived that describes the relationship between the duty cycle ratio, the inductor current, and the input and output voltage.

$$V_{L_{on}} = V_i - V_o \quad (2.1)$$

$$t_{on} = DT \quad (2.2)$$

$$\frac{dI_L}{dt} = \frac{V_i - V_o}{L} \quad (2.3)$$

$$\Delta I_{L_{on}} = \Delta t_{on} \cdot \frac{V_i - V_o}{L} \quad (2.4)$$

$$\Delta I_{L_{on}} = \frac{DT(V_i - V_o)}{L} \quad (2.5)$$

V_{Lon} is the voltage across the conductor in ON mode, V_i is the input voltage, V_o is the output voltage across the resistive load, L is the inductance of the inductor, t_{on} is the duration for which the converter is in ON mode for a single cycle, D is the duty cycle ratio, $\Delta I_{L_{on}}$ is the ripple current across the inductor and T is the total time period. During this cycle, there is no current flowing through the diode [33].

However, once the switch is opened and the OFF mode begins, the current in the inductor flows through the diode and charges the output capacitor. During OFF mode, the switch is open and the inductor's polarity is reversed, making it a voltage source. The magnetic field in the inductor collapses and causes a discharge of current in the inductor. The voltage across the inductor now equals the load voltage but with the polarities reversed, i.e., $V_L = -V_o$. The duration for which the converter is in the OFF mode can be determined using the following equation:

$$t_{off} = (1 - D)T. \quad (2.6)$$

t_{off} is the duration for which the converter is in OFF mode for a single cycle. Similarly to the ON mode, the ripple current in the inductor can be determined, providing the relationship between duty cycle ratio, inductor current, and the output voltage [33].

The buck converters ON and OFF modes can be switched rapidly to generate a constant DC voltage. The inclusion of a capacitor helps to smooth out the output voltage and produce a usable voltage signal. The transfer function, or the relationship between the input and output voltage, is defined as

$$\frac{V_o}{V_i} = D. \quad (2.7)$$

This means that the output of the buck converter can be controlled by adjusting the duty cycle ratio of the switch [33].

DC-DC Boost Converter

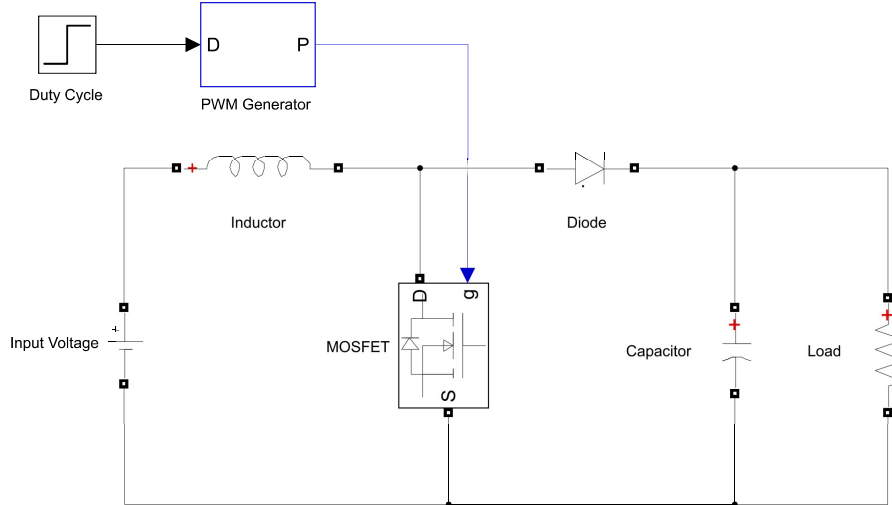


Figure 2.3: DC-DC Boost Converter.

The boost converter is a type of DC-DC converter that is used to step up or increase the input voltage to a higher voltage level. The boost converter circuit is similar to that of the buck converter and operates in two modes - the ON mode and the OFF mode. During the ON mode, the switch is closed and the voltage across the inductor is the same as the input voltage. $V_L = V_i$ However, no current flows through the inductor during this mode. By using the voltage and current relationship for an inductor, we can derive the equation for the rippling current in the inductor and the input voltage [34].

$$\frac{dI_L}{dt} = \frac{V_i}{L} \quad (2.8)$$

With the inclusion of time and duty cycle ratio, it is possible to obtain an expression for the relationship between duty cycle ratio, input voltage, and inductor current, similar to the buck converter [34].

$$\frac{dI_L}{dt} = \frac{\Delta I_L}{\Delta t} = \frac{\Delta I_L}{DT} = \frac{V_{in}}{L} \quad (2.9)$$

When the boost converter is in OFF mode, the switch is open and the magnetic field in the inductor collapses. The diode is closed and current flows through it. As the magnetic field collapses, the polarity of the inductor is reversed, and it becomes a source of voltage. The inductor current equals the current across the capacitor and the resistive load. $I_L = I_C + I_R$. Similar to the buck converter, the voltage across the inductor equals the voltage difference between the input voltage and the voltage across the resistive load. $V_L = V_i - V_o$. The

expression for the duty cycle ratio is given by. The relationship between the duty cycle ratio, input and output voltage can be obtained using the voltage and current relationship for an inductor. The final relationship between the input and output voltage is given by:

$$\frac{V_o}{V_i} = \frac{1}{1 - D}. \quad (2.10)$$

This relationship also shows that the output voltage will always be greater than the input voltage [34].

DC-DC Buck-Boost Converter

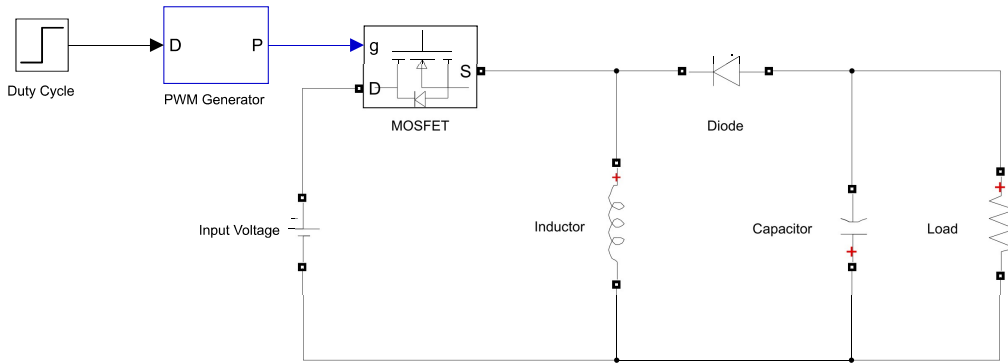


Figure 2.4: DC-DC Buck-Boost Converter.

The buck-boost converter is another DC-DC boost converter which works according to the same principles as the buck converter and boost converter. The buck-boost converter is a combination of the buck converter and the boost converter where it uses the capabilities of both systems to step-up and step-down the voltage level. The buck-boost converter also has two modes of operation – the ON mode and the OFF mode. In the ON mode the current flows through the inductor and not through the rest of the circuit as the diode is in an open position. In this stage the inductor builds up a magnetic field as seen in the previous circuits of buck and boost converter. The input voltage and the voltage across the inductor are the same. $V_i = V_L$. The relationship between the input voltage, inductance, the rippling current and the duty cycle ratio can be obtained from the voltage current relationship of the inductor [35].

As the switch is turned off and the converter is in OFF mode, the polarity of the inductor is reversed and acts as a voltage source thereby charging the capacitor. Here, the output voltage is the same as the inductor voltage. The relationship between the output voltage, duty cycle ratio and the rippling current can also be obtained using the same methods

used for other converters. The final transfer function shows the input output relationship between the input voltage, output voltage and the duty cycle ratio:

$$\frac{V_0}{V_i} = \frac{-D}{1-D}. \quad (2.11)$$

It can be inferred from the above equation that the converter behaves as a buck converter for duty cycle ratios below 0.5 and as a boost converter for duty cycle ratios above 0.5 [35].

The power electronics circuits briefly mentioned above are key to bridging the PV module and the electrolyser. This initial background of DC-DC converters provides a good foundation for modelling the relationship and open up the possibilities of control where the output voltage and current can be modified according to requirements set by the PV module and the electrolyser being used.

2.5 Problem Delimitation

After analysing the available technologies and algorithms pertaining to solar, hydrogen and converter systems, a problem defining the focus of this report can be formulated: **How to develop a control system that can maximise or optimise hydrogen production through solar energy conversion?** This problem statement opens up opportunities to analyse, model, simulate, and control hydrogen production through solar energy conversion. It also provides a framework for comparing and evaluating the influence of voltage and current on the production of hydrogen.

2.5.1 Electrolyser Choice

There is a range of factors that can be taken in consideration when choosing an electrolyser. As described in the Table 2.1, there are three main types based on the electrolyte material. One of the main criteria is to find a system that is cost-effective with widely-available, commercial components, therefore the Solid Oxide electrolyser is discarded because it is a technology still on the development stage. Furthermore, most of its applications are based on combinations with constant current supplies, such as nuclear power plants [36], which help the electrolyser to not incur thermal stress. Further research on the combination of Solid Oxide assemblies with fluctuating renewable sources is being conducted with deep learning techniques [37], which are beyond the scope of the project.

Comparing the Alkaline and the Proton Membrane Exchange electrolyser, the latter presents several advantages such as high-power density and better response to source fluctuations. Despite these advantages, the use of noble metals increases the cost and hinders its commercialisation possibilities. Additionally, the instability of the polymer membrane inside

an acidic media shortens the lifetime of the component, which decreases the return of investment.

The cost of an alkaline electrolyser, including installation, in 2017 was of about 750 € per kW, while the PEM counterpart required a disbursement of 1200 € per kW. Both prices are expected to decrease by 2025, to an estimated of 480 € per kW versus 700 € per kW [38]. Additionally to the economical factor, there is a smaller production capacity of PEM assemblies across different manufacturers, which usually offer PEM stacks under the MW scale, while most of the Alkaline counterparts surpass this mark [39]. Alkaline electrolyzers have the potential to become a readily available option for off-grid setups, therefore it is chosen as the assembly to develop the model around.

2.5.2 MPPT Algorithm Choice

To ensure work on the highest possible power level, an MPPT algorithm needs to be chosen and implemented. The described MPPT algorithms differ when it comes to effectiveness and complexity. In this semester project, however, the group decided to work with the P&O algorithm as it is a well-established and widely used technique to track the maximum power point of any photovoltaic system. Its ease of implementation and maintenance, as well as effectiveness and performance under steady-state conditions, make it a justifiable choice for this semester project.

2.5.3 DC-DC Converter Choice

Based on the parameters of the PV module with an MPPT charge controller and the electrolyser, the controllable elements can be identified as the voltage and current input to the electrolyser. By controlling these parameters, it is possible to optimize hydrogen production. To control the input voltage and current to the electrolyser, the voltage from the PV module and the MPPT charge controller can be passed through a DC-DC converter, such as a boost converter. It is worth noting that the voltage output of the MPPT charge controller can vary depending on irradiance and temperature.

Chapter 3

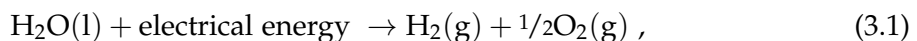
Problem Solution

Following the problem delimitation and formulation in section 2.5, the problem solution section aims to develop a solution to the proposed problem formulation. Models for the three main parts of the system - electrolyser, PV cell with MPPT, and DC-DC boost converter are identified using various techniques. A control system for the identified DC-DC boost converter model is developed. The models are integrated and simulated with existing and widely used software such as MATLAB and Simulink. The controller is then tested against a real system for validation.

3.1 Modelling

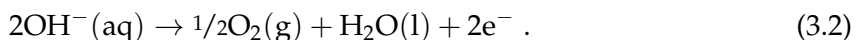
3.1.1 Alkaline Electrolyser

The net reaction for splitting the water with an alkaline electrolyser is [40]:

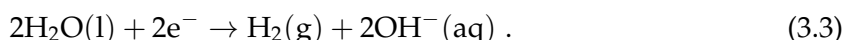


while the electrochemical half-reactions are:

At the anode:



At the cathode:



Where (l) stands for liquid, (g) for gas, and (aq) for water-based solution.

In order to produce this reaction, a minimum voltage should be applied to the electrodes, which is also known as reversible voltage (V_{Rev}). In an ideal scenario, cell voltage is equal to V_{Rev} , but due to irreversibility, the cell voltage is higher in practice. This added voltage, referred as overvoltage, and represents the additional driving force required to overcome barriers and create the gas.

Another relevant parameter in the electrolyser is the ohmic resistance (r), which refers to the resistance encountered by the current through the electrolyte solution and the electrode surfaces. This parameter is determined by the conductivity of the electrolyte, which depends on several factors, including its concentration and temperature.

The electrode kinetics of an electrolyser cell can be modelled using empirical current–voltage (I–V) relationships [41]. The basic form of the equation is:

$$V = V_{Rev} + \frac{r}{A}I + s * \log\left(\frac{t}{A}I + 1\right). \quad (3.4)$$

Linearisation and Electrical Equivalent

One of the important criteria of this project is that the electrolyser can be electrically modelled. This in order to implement a physical solar panel, MPPT, converter, and controller. As the main focus is the control aspect of the project, testing using an actual electrolyser during physical testing was deemed unnecessary. Thus, an electrical equivalent model was developed. In order to utilise simple electrical components which operate in a linear manner according to Ohm's law, it was necessary to linearise the equation relating input current to the cell voltage. the linearisation was done using a first order Taylor series, defined mathematically for the cell voltage equation as:

$$f(I) = \sum_{k=0}^1 V^{(k)}(a) \frac{(I - a)^k}{k!}, \quad (3.5)$$

where a is a specific point I for the function $V(I)$ at which the linearisation is performed, and

$$V(I) = V_{Rev} + \left(\frac{(r_1 + r_2 * T)}{A} * I + s * \log\left(\frac{(t_1 + t_2)}{T} + \frac{t_3}{T^2}\right) * \frac{I}{A} + 1 \right). \quad (3.6)$$

The parameters used for the equation were the following:

- $V_{Rev} = 1.29 \text{ V}$
- $r_2 = -3.02150 * 10^{-6} \frac{\Omega m^2}{^\circ\text{C}}$
- $r_1 = 3.53855 * 10^{-4} \Omega m^2$
- $s = 0.22396 \text{ V}$

- $t_1 = 5.13093 \frac{m^2}{A}$
- $t_2 = -2.40447 * 10^2 \frac{\text{ }^\circ\text{C} m^2}{A}$
- $t_3 = 3.410251 * 10^3 \text{ }^\circ\text{C}^2 \frac{m^2}{A}$
- $T = 25 \text{ }^\circ\text{C}$
- $A = 0.01 \text{ } m^2$

Equation 3.6 and its associated parameters are taken from a study which focused on simulation and modelling of an electrolyser [42]. The linearisation point chosen was at $I = 32.5 \text{ A}$, corresponding to operating at 4 V per cell. This was fitting as the operating voltage would be 400 V or higher, and the simulation to be run on 100 series cells.

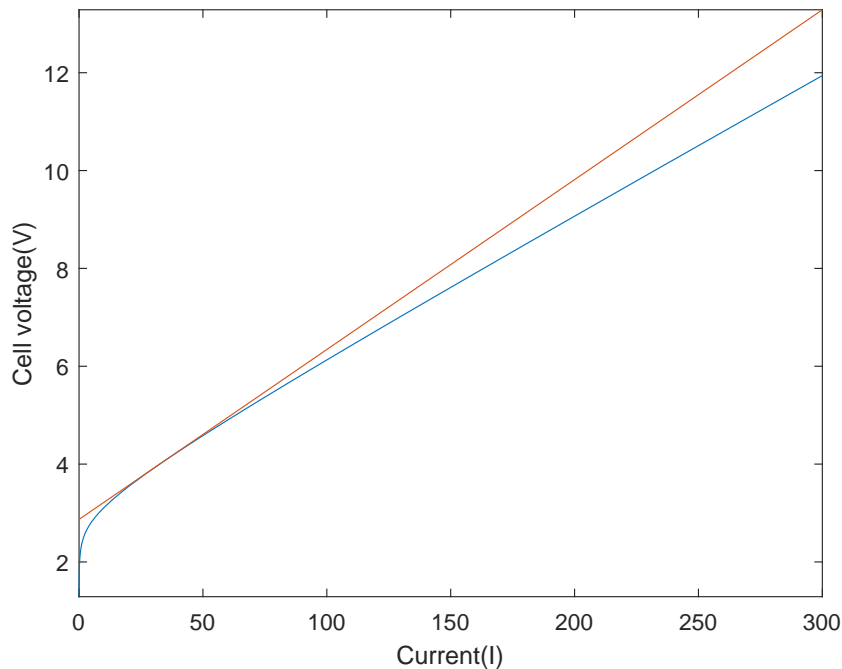


Figure 3.1: The figure displays the mathematical model(blue) and the linearised model(orange) of the electrolyser.

The graph shows that for a quite large range of current the linearisation is close to the model. Since it is linear, the slope of the curve can be modelled electrically by a resistor. However, the trade-off is the point at which the current is zero, where it intersects at $V = 2.87 \text{ V}$. Modelling the reversible voltage using a voltage source will thus have to be set at this value, which is higher than the actual reversible voltage of an electrolyser cell.

The slope of the curve is 0.034, which is the electrically equivalent resistance per cell. The electrical equivalent is thus built up in the following manner:

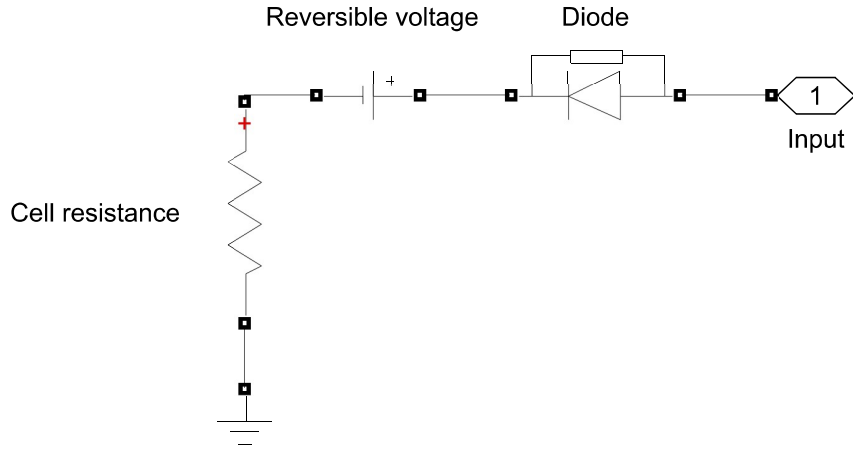


Figure 3.2: The electrical equivalent model of an electrolyser.

The scheme shows one single cell, however, given the linearity of Ohm's law, scaling up to the desired 100 cells is a matter of multiplying the cell resistance and reversible voltage by 100. The final value of the total cell resistance is thus 3.4Ω and the reversible voltage 287 V. The diode added is to ensure no current is induced until V_{in} is larger than the reversible voltage. For the simulation in section 3.2 only the resistive part of the electrolyser model is used, as the main concern was that of voltage regulation and MPPT boosting. In the physical implementation the model described in chapter 4.1 a high resistance not based on the electrolyser model was used, to lower the amount of current.

3.1.2 PV Cell and MPPT Algorithm

As mentioned in section 2.5.2, the MPPT algorithm of choice is Perturb and Observe. The complete behaviour of the algorithm is presented in figure 3.3.

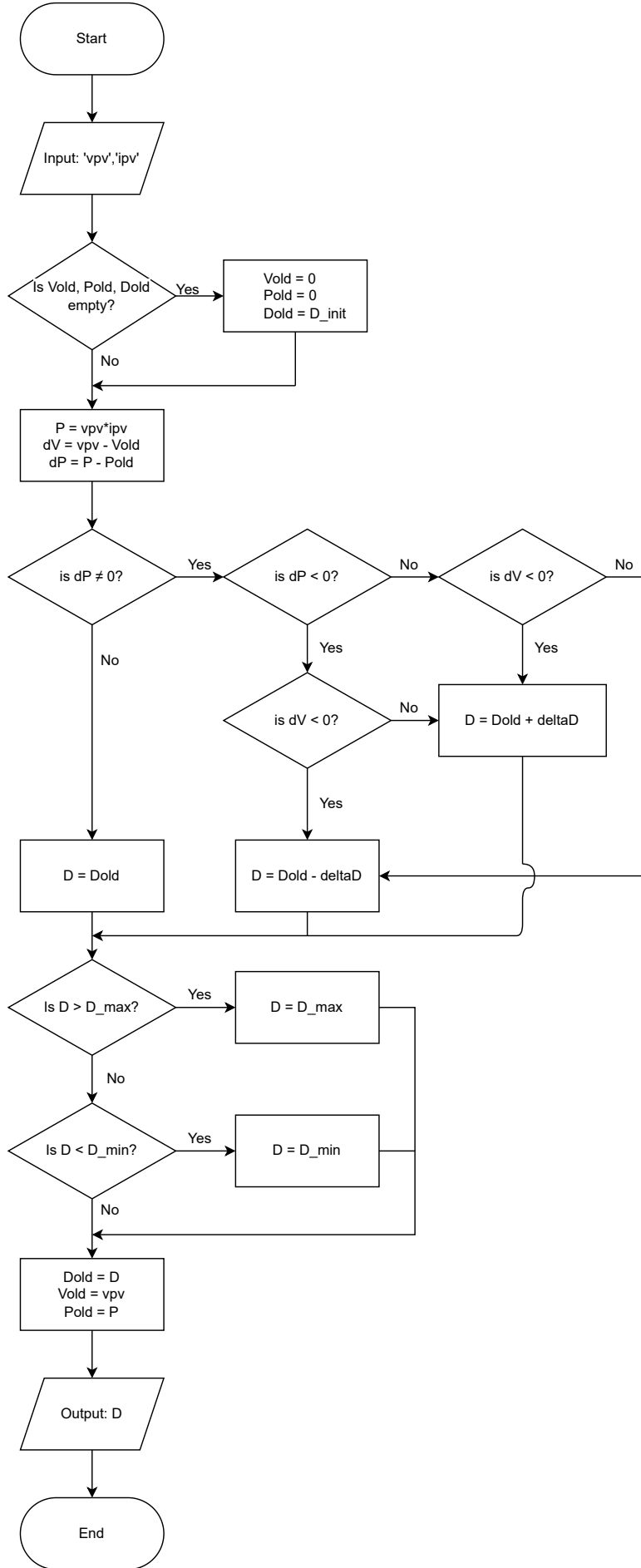


Figure 3.3: Description of the process of determining a proper value for duty cycle, which ensures the highest power draw from the photovoltaic cell.

Listing 1: MPPT function definition

```
1 function D = fcn(vpv, ipv)
```

This line of code defines a function called **fcn** which takes as input the instantaneous values of voltage (vpv) and current (ipv) coming from the PV cell and returns the duty cycle value (D) as output.

Listing 2: MPPT constants

```
1 D_init = 0.4;
2 D_max = 0.9;
3 D_min = 0.1;
4 deltaD = 20e-6;
5 persistent Vold Pold Dold;
```

The assigned constants indicate the initial, maximum and minimum duty cycle values, which were defined in order to ensure the best stability and efficiency of the system, as well as the small change in the duty cycle value which is either added or subtracted from the old value. **Vold**, **Pold**, and **Dold** are persistent variables which serve as the old values of the PV voltage, power and duty cycle value respectively. They are used to calculate the actual changes in voltage and power.

Listing 3: MPPT initial values

```
1 %Assign starting values
2 if isempty(Vold)
3     Vold = 0;
4     Pold = 0;
5     Dold = D_init;
6 end
```

When the algorithm runs for the first time, the initial values of old voltage, power and duty cycle should be set to 0 as they have not been assigned to anything.

Listing 4: MPPT change in power and voltage

```
1 P = vpv*ipv;
2 dV = vpv - Vold;
```

```
3 dP = P - Pold;
```

Instantaneous power (P) is calculated by multiplying the instantaneous voltage and current. Subsequently, the change in voltage and power is obtained. It is done in order to be able to define the behaviour of the algorithm.

Listing 5: MPPT Perturb and Observe method

```
1 if dP ~= 0
2   if dP < 0
3     if dV < 0
4       D = Dold - deltaD;
5     else
6       D = Dold + deltaD;
7   end
8 else
9   if dV < 0
10    D = Dold + deltaD;
11  else
12    D = Dold - deltaD;
13  end
14 end
15 else
16   D = Dold;
17 end
```

This block of code represents the P&O algorithm. If there is any change in power, the algorithm analyses four possible cases:

1. If $dP < 0$, $dV < 0$, then decrease the duty cycle value
2. If $dP < 0$, $dV \geq 0$, then increase the duty cycle value
3. If $dP \geq 0$, $dV < 0$, then increase the duty cycle value
4. If $dP \geq 0$, $dV \geq 0$, then decrease the duty cycle value

If there is no change in power, the duty cycle value should not be changed.

Listing 6: MPPT duty cycle values

```

1 if D > D_MAX
2   D = D_MAX;
3 elseif D < D_MIN
4   D = D_MIN;
5 end

```

This piece of code checks whether the new duty cycle is within specified boundaries. If it is outside its limits, the old duty cycle value is used instead.

Listing 7: MPPT assigning old values

```

1 Dold = D;
2 Vold = vpv;
3 Pold = P;

```

When the whole code is executed, the instantaneous values become old values and the whole circle repeats one more time. This exploit allows to constantly check for the new optimum value of the duty cycle which will improve the overall efficiency of the power transfer.

3.1.3 Modelling and Control of Boost Converter

Identification of the Transfer Function

In order to control the voltage to the electrolyser, it is necessary to derive a transfer function of the boost converter, upon which a controller can be tuned. The transfer function of interest is that of a voltage input to a duty cycle output, so as to manipulate the duty cycle to the switching device in the converter. A general form transfer function which applies to buck, boost and buck-boost converters is given by [43]:

$$G_{vd}(s) = G_{d0} \frac{1 - \frac{s}{\omega_z}}{1 + \frac{s}{Q\omega_0} + (\frac{s}{\omega_0})^2}. \quad (3.7)$$

Specifying this to a boost converter transfer function, specific equations are given for G_{d0} , ω_0 , ω_z , and Q . These are as follows [43]:

$$G_{d0} = \frac{V}{1 - D}, \quad \omega_0 = \frac{1 - D}{\sqrt{LC}}, \quad \omega_z = \frac{R(1 - D)^2}{L}, \quad Q = R(1 - D)\sqrt{\frac{C}{L}}, \quad (3.8)$$

where V is the output voltage to the circuit, D is the duty cycle calculated for the desired output voltage, L the inductance of the boost converter, C the capacitance of the boost

converter, and R the load of the system, here being the electrolyser model functioning at 3.4Ω . The duty cycle value is calculated using some assumption on the input voltage, and a desired set output voltage. The desired output voltage is 400 V, and since the voltage will always be boosted, the solar panel dimensions are set as such that they can produce 400 V maximum. An assumption that the average input voltage would be 200 V was made for calculation purposes. The general equation for calculating D is [44]:

$$V_{out} = \frac{V_{in}}{1 - D}, \quad (3.9)$$

where solving for D with the above values gives a duty cycle of

$$D = 0.5. \quad (3.10)$$

The inductance and capacitance were derived using the following equations [45]:

$$L \geq \frac{V_{in}DT}{I_{in}\delta}, \quad (3.11)$$

$$C \geq \frac{DTI_{out}}{V_{in}\delta}. \quad (3.12)$$

Where T is the ripple period and δ is the ripple voltage. In other words, how much the voltage changes in the capacitor or inductor during a given time period. The values used to calculate L and C are $I_{in} = 250 A$, $I_{out} = 125 A$, $D = 0.5$ and $V_{in} = 200 V$, giving the L and C values:

$$L \geq 0.04 H, \quad C \geq 0.03 F. \quad (3.13)$$

As they are to be greater than these values, they were rounded up to sizes that seemed sufficient, and were tested and functioning in simulation. The final values determined for L and C:

$$L = 0.05 H, \quad C = 0.2 F. \quad (3.14)$$

Using D, L, C and R, the equations 3.8 were determined and inserted into the general form transfer function, giving the final transfer function to be the following:

$$G_{vd}(s) = \frac{-20000s + 340000}{17s^2 + 25s + 425}. \quad (3.15)$$

Open Loop Analysis

To better understand the behaviour of the system, it is crucial to perform an open-loop analysis. By doing so, the group is able to determine if the system is stable, has an inverse response, see how the system responds to different input signals and also it allows to design a closed-loop system in an easier manner.

Stability

The zeros are the values of s when the numerator of the equation 3.15 is equal to zero. In this case the value of s is equal to 17. It is located on the right-half side of the plane.

The poles are the values of s when the denominator of the same equation is equal to zero. In this case the values of s are equal to $-0.7353 - 4.9456i$ and $-0.7353 + 4.9456i$ as shown in figure 3.4. The poles are located on the left-half side of the plane because of their negative real part, which indicates that the system is stable. However, the poles are located close to the imaginary axis which results in slower response as if they were further away from the imaginary axis to the left.

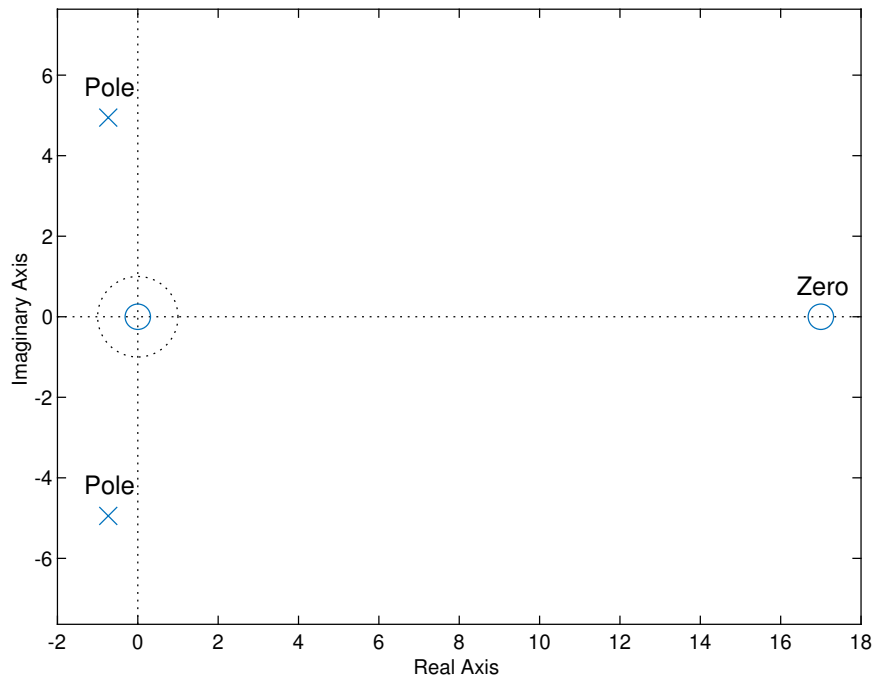


Figure 3.4: Pole-Zero map of transfer function 3.15.

DC Gain

The DC gain of a system is the steady-state value of the unit step response of this system. It can be found by setting the input frequency to zero.

By setting the Laplace variable s to zero in the equation 3.15, the DC gain of the system is obtained and is equal to 800. Therefore, when the input to the system is a constant signal, the output will be amplified by 800 in the steady-state open loop system.

Step Response

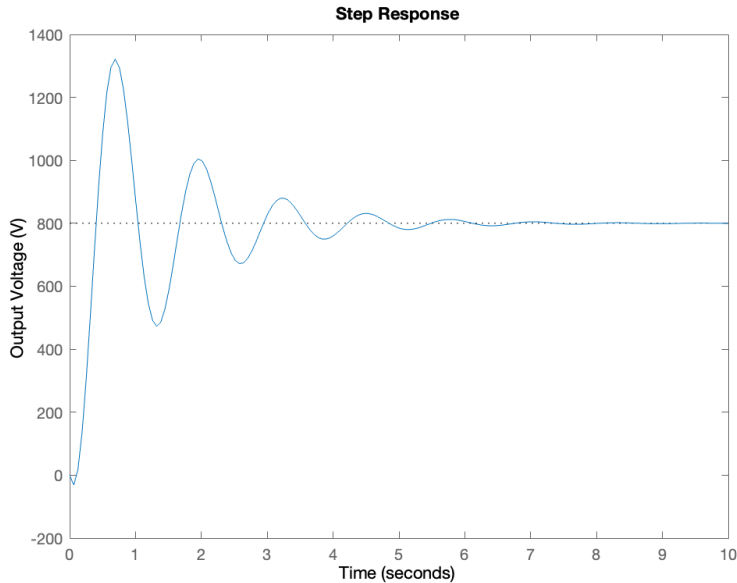


Figure 3.5: Step response of the open-loop transfer function $G_{vd}(s)$

The step response of the open-loop transfer function can be seen in figure 3.5. The system oscillates a bit, however it settles down after around 6 seconds and is stable.

Natural Frequency

The natural frequency of a system is the vibration speed a system has. It can be found by calculating the magnitude of the poles, or simply by the following equation:

$$H(s) = \frac{w_n^2}{s^2 + 2\xi w_n s + w_n^2} . \quad (3.16)$$

Where ξ is the damping ratio, and w_n is the natural frequency. In order to find the natural frequency from the equation 3.15, the denominator needs to be changed to this form, and after that, it turns out to be 5 rad/s.

Damping Ratio

The damping ratio is a parameter that describes the level of damping in the system, which determines how quickly the system responds to changes in input and how much it oscillates around its steady-state value. It can also be obtained from the equation 3.16, and in this case, it has a value of 0.1471. Since this number is between zero and one, it is an underdamped system, which means that it will oscillate around its steady-state value with a frequency that is higher than the natural frequency of the system.

Resonance Frequency

The resonance frequency of a system is the frequency at which the system's response to an input becomes maximum, assuming the input frequency is varied. For a damped system, it can be calculated using the following equation:

$$w_r = w_n \sqrt{1 - \xi^2}, \quad (3.17)$$

where w_r is the resonance frequency, $w_n = 5$ rad/s and $\xi = 0.1471$. For this system, it has a value of 4.9457 rad/s.

Rising Time

The rising time of a system is the time it takes for the output to rise from 10% to 90% of its final value. It is calculated by the formula:

$$T_r \approx \frac{1.8}{w_n}. \quad (3.18)$$

By this formula, the rising time of the chosen system is 0.3640 s if $w_n = 5$ rad/s.

Peak Time

It is the time it takes for the output of the system to reach its first peak, above the steady-state value, after the input has been applied. From the natural frequency and the damping ratio, it can be determined by:

$$T_p = \frac{\pi}{w_n \sqrt{1 - \xi^2}}. \quad (3.19)$$

After the respective calculations, the peak time of the system turns out to be 0.6352 s for $\xi = 0.1471$ and $w_n = 5$ rad/s.

Settling Time

The settling time is a parameter used to describe the time it takes for a system's response to settle within $\pm 1\%$ to 5% deviation around its final steady-state value, in response to a step input. If $0 < \xi < 0.69$, the settling time of the system is calculated by:

$$T_s \approx \frac{3.1}{\xi w_n} . \quad (3.20)$$

For this system, the value of the settling time is 4.354 s if $\xi = 0.1471$ and $w_n = 5$ rad/s.

Maximum Overshoot

The maximum overshoot of a system is a parameter used to describe the maximum amount by which a system's response exceeds its final steady-state value, in response to a step input. It is typically expressed as a percentage of the final value and is the difference between the maximum peak of the response and the final steady-state value. It is calculated using the equation:

$$M_p = e^{\frac{-\xi\pi}{\sqrt{1-\xi^2}}} \% . \quad (3.21)$$

In this case, when $\xi = 0.1471$ the maximum overshoot of the system is 62.70 %

Bode Plot

A Bode plot is a graph that shows the frequency response of a system or circuit. It normally does that by expressing the magnitude and phase as a function of frequency. The magnitude of the frequency response is typically represented on a logarithmic scale and expressed in decibels (dB), while the phase is typically represented in degrees. These two values are shown in two plots, one for the phase response and the other for the magnitude response. They can also be used to design and optimise systems and circuits for specific applications, such as filtering, amplification, and control. For the system, the Bode plot was determined and it is the following:

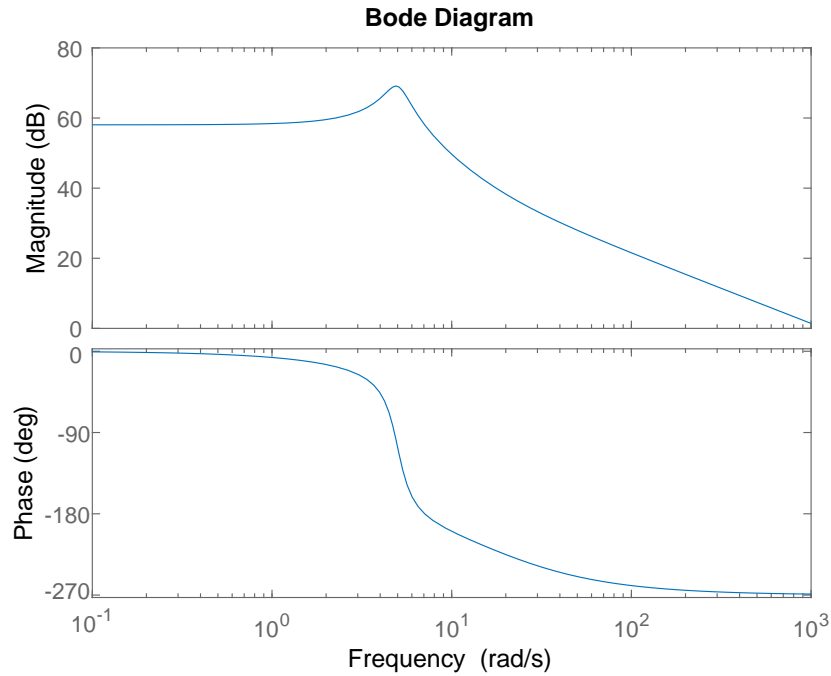


Figure 3.6: Bode plot of transfer function 3.15.

From the Bode plot, the stability margins can be found. These margins are the Gain and Phase margins. The gain margin is a parameter used to describe the amount of gain that can be added to a system or circuit before it becomes unstable. It is the difference in dB between the magnitude and 0 dB on the bode plot at the frequency where the phase is -180° . In this system, the gain margin is -58.1 dB at 7.07 rad/s. This means that it is already close to the stability limit and may become unstable if additional gain is added.

The phase margin is typically expressed in degrees and is defined as the difference between the phase shift at the frequency where the magnitude of the system's transfer function is unity and -180° , which represents the phase shift required for the system to become unstable. In the system, the phase margin is found at $1.18e^3$ rad/s, and it is of -89.1° . This means that the system is more likely to become unstable if additional phase shift is added and can exhibit oscillations or instability under certain conditions. There is a delay margin of 0.00402 s.

Closed Loop Analysis

In order to achieve the desired output, the feedback branch is introduced. It allows measurement of the actual output of the system and comparing it with the desired output value. By subtracting the actual output from the reference value, an error value is fed to the input of the system which allows the system to self-regulate.

The closed loop transfer function of the system is obtained by applying Mason's rule, which allows the derivation of a new transfer function with the feedback branch included.

$$H(s) = \frac{G_{vd}(s)}{1 + K \cdot G_{vd}(s)}, \quad (3.22)$$

where K is the feedback gain.

After setting the K value to 1, the new obtained transfer function is given by:

$$H(s) = \frac{-20000s + 340000}{17s^2 - 19975s + 340425}. \quad (3.23)$$

The closed loop transfer function 3.23 has exactly the same zero location as the open loop transfer function 3.15 located at s being equal to 17.

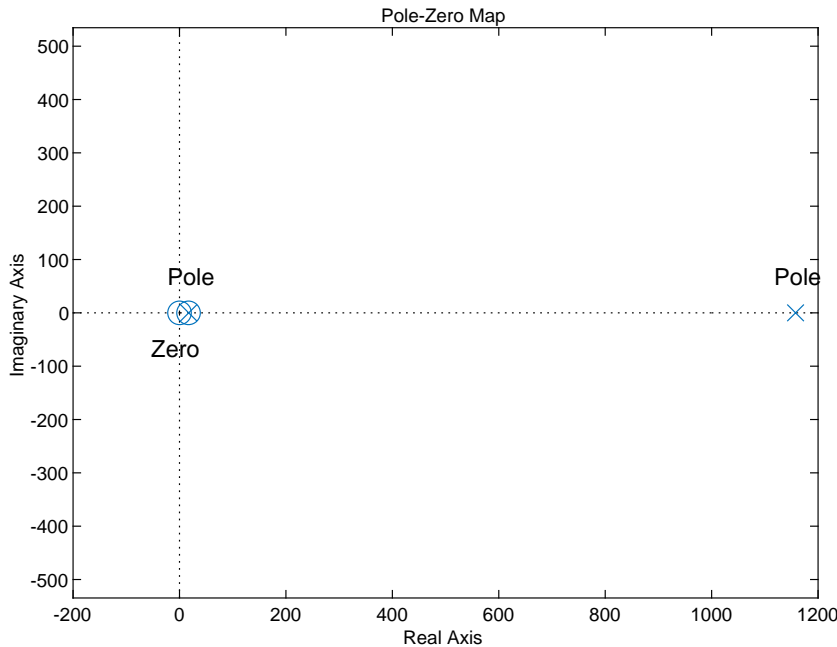


Figure 3.7: Pole-Zero map of the closed-loop transfer function 3.23.

The poles of the newly derived transfer function are real and located at s equal to 17.2972 and 1157.7028 as shown in figure 3.7. The poles are located on the right-half side of the plane, which indicates that the system is unstable.

To achieve the desired stability, the root locus method can be applied. It allows to find the feedback gain values which would make the system stable and robust.

Step Response

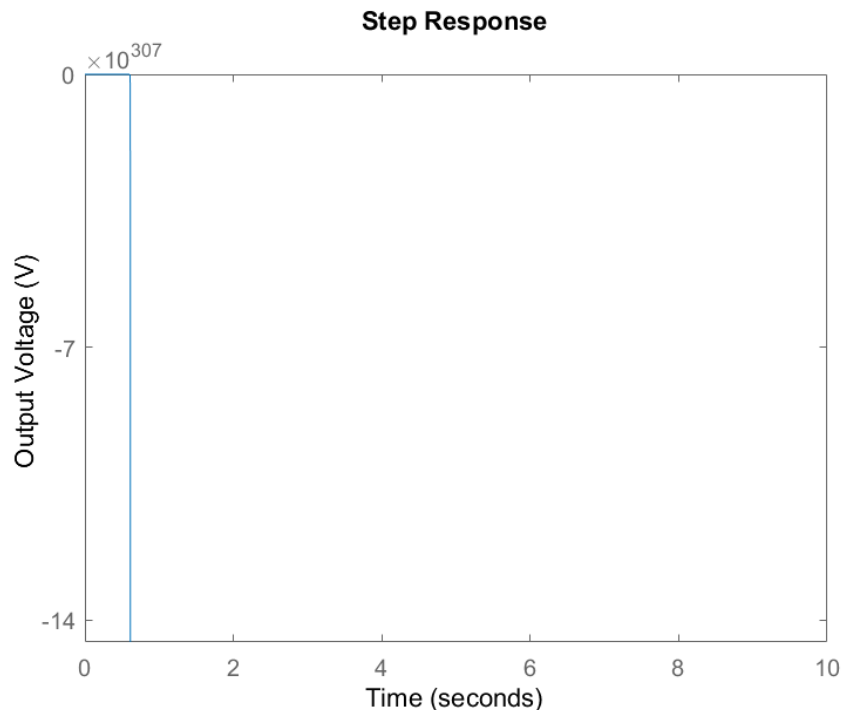


Figure 3.8: Step response of the closed loop transfer function $H(s)$ with the feedback gain set to 1.

It can be seen from the step response of $H(s)$ in figure 3.8 that the system is unstable and that a controller is required to make the system stable.

Root Locus Analysis

Root locus analysis can be performed on the obtained boost converter model. The feedback gains and the corresponding pole values are obtained. The transfer function of the system with feedback containing a feedback gain K is found using Mason's rule in equation 3.22.

The expanded equation is given by:

$$H(s) = \frac{-20000s + 340000}{17s^2 + s(25 - 20000K) + 425 + 340000K}. \quad (3.24)$$

From equation 3.24 the characteristic equation (the denominator) can be used to find the poles of the system, thereby identifying the poles for a given value of K. The roots of the characteristic equation are found to be:

$$s = \pm \frac{5}{34} (\sqrt{16000000K^2 - 964800K - 1131} - 4000K + 5) \quad (3.25)$$

Using the equation 3.25, the root locus plot of the system can then be formed with different values of feedback gain K.

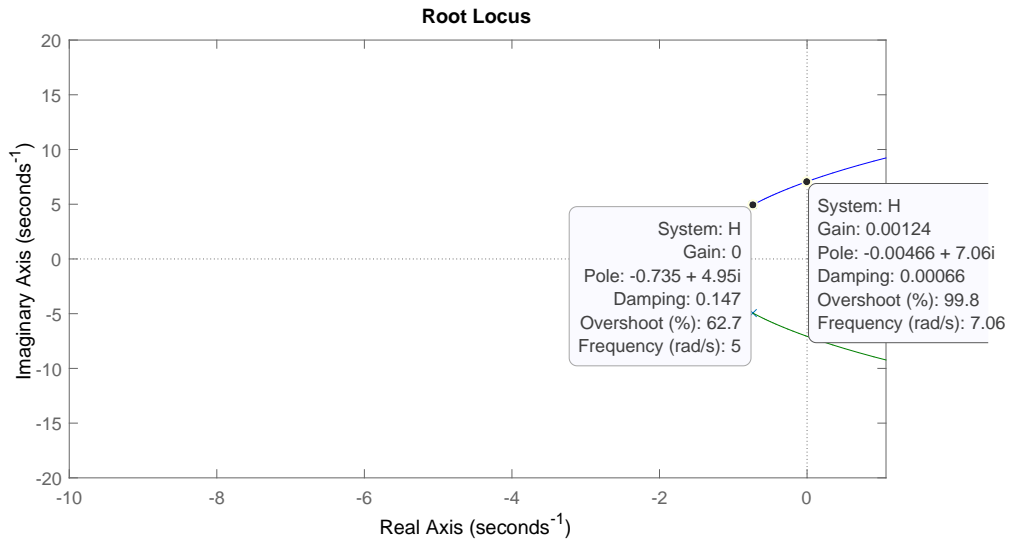


Figure 3.9: Root locus plot of transfer function H(s) showing the range of feedback gain values where the system is stable.

The stability of the system can be studied for various values of K. For feedback gain values equal to and above 0.00125, the system is unstable. Therefore, according to the root locus analysis, a feedback gain K equal to or less than 0.00124 and greater than 0 has to be used in order to have a stable system. The settling time and the gain used are proportional. The lower the gain, the lower the settling time and the system reaches steady state value quicker. In order to be able to calculate the time properties of the system, the chosen value of K will be 0.0001.

DC gain

To calculate the DC gain of the system, the same method as in the open circuit must be used. After substituting the value of the feedback gain for 0.0001, the DC gain turns out to be 740.7.

Natural Frequency

To determine the natural frequency of the system, the equation 3.16 must be used. After all the calculations, the value of the natural frequency is 5.1962 rad/s.

Damping ratio

The damping ratio is calculated the same way as in the open loop analysis, which is using the equation 3.16. Then, the damping factor of this system is of 0.1302.

Resonance Frequency

The resonance frequency is calculated using the equation 3.17, and it ends up being 5.1521 rad/s.

Rising Time

To get the rising time of the system, the equation 3.18 must be used. This rising time will be of 0.3464 s.

Peak Time

The equation 3.19 must be used to determine the peak time of the system. Finally, the value of the peak time for the system is 0.6098 s.

Settling Time

The settling time of the closed loop system is determined using the equation 3.20, and it has a value of 4.7371 s.

Maximum Overshoot

To calculate the maximum overshoot of the system, the equation 3.21 is used. This procedure gives a final value of 66.24 % of overshoot.

Bode Plot

The Bode diagram of the closed-loop system of 3.24 shows the following frequency response diagram:

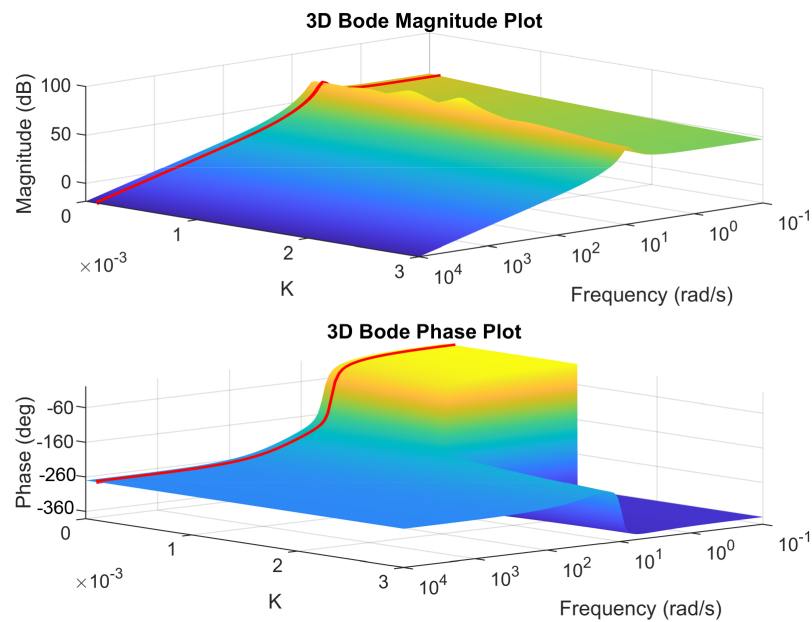


Figure 3.10: Bode plot of transfer function 3.24 for a range of values of K.

In this three-dimensional diagram, the whole range of bode plots of values of K from 0 to 0.003 is represented. Although some negative values of the feedback gain are also considered stable, it is only taken into account the range obtained from the root locus. The red line indicates the plot of the specific case treated in figure 3.11, when K has a value of 0.0001, and it is able to demonstrate in the phase plot that when K is greater than 0.00124, it loses stability as there is an abrupt change in the shape of the plot.

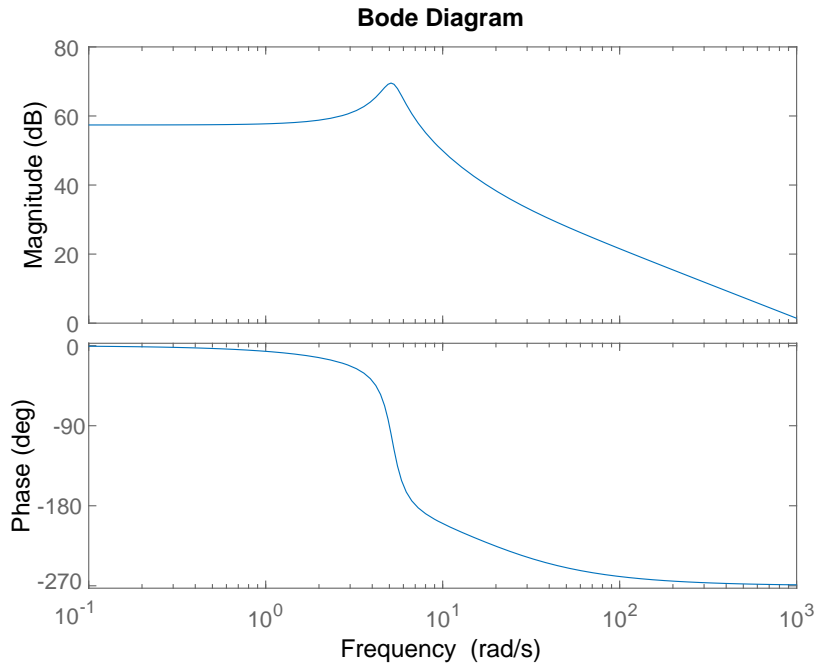


Figure 3.11: Bode plot of transfer function 3.24 with $K=0.0001$.

This is the bode plot for when the value of K is 0.0001. In this diagram, there is a negative gain margin of -58.8 dB at 7.07 rad/s. This means that the system will lose stability as the feedback gain K increases, which means that it will oscillate more when the closed-loop step response is calculated. The phase margin is also negative, and it has a value of -89.1° . This indicates that the system is almost unstable, and small changes in the system could cause instability. A negative phase margin typically means that the closed-loop system is likely to be unstable, and it suggests that the system needs further tuning or modification to increase stability.

3.1.4 Control

The objective of the control of the boost converter is to stabilise the output voltage of the converter to a steady state value. This project describes the control of the boost converter for an input voltage of 200 V and an output voltage of 400 V. Parameters for inductance, capacitance, duty cycle, input current, output current, ripple current, ripple voltage, and duty cycle are mentioned in section 3.1.3. The linearised model is most accurate for the above-mentioned parameters and specifications for the chosen boost converter.

Based on the linear properties of the identified transfer function model a Proportional-

Integral-Derivative (PID) controller can be used to control the output voltage with input as the duty cycle.

The transfer function $G_c(s)$ for a PID controller with K_p as the proportional gain, K_i as the integral gain, and K_d as the derivative gain is as follows:

$$G_c(s) = K_p + \frac{K_i}{s} + K_d s . \quad (3.26)$$

The transfer function of the PID controller and the transfer function of the boost converter can be combined with a feedback gain as seen in 3.12.

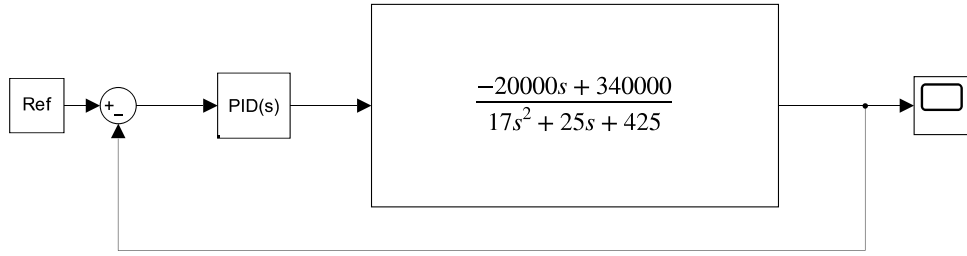


Figure 3.12: Block diagram of closed loop transfer function with PID controller.

The resulting transfer function $H_c(s)$, which denotes the relationship between the output voltage and reference voltage with $G_c(s)$ as the transfer function of the PID controller, $G_{vd}(s)$ as the transfer function of the boost converter, V_o as the output voltage and V_{ref} as the reference voltage is given by

$$H_c(s) = \frac{V_o}{V_{ref}}(s) = \frac{G_c(s)G_{vd}(s)}{1 + G_c(s)G_{vd}(s)} . \quad (3.27)$$

Identifying controller coefficients

A process of manual tuning is performed to identify the controller coefficients. The proportional gain K_p is found from the root locus analysis in section 3.1.3. The value of K_p has to be less than or equal to 0.00124 and greater than zero for the system to be stable. At values close to 0.00124, the response of the system displays many oscillations and to correct this, a smaller value of K_p is used. For $K_p = 0.0001$, the response of the system displays some oscillations and it is also able to stabilize faster than the systems with a higher value of K_p . The value of K_p is set at 0.0001 and for lower values, the steady state error is larger. To correct the steady state error in the response of the system when $K_p = 0.0001$, an integral gain K_i is used. Initially, K_i is set to 0.0001 and after a process of slowly increasing

the value of K_i , the best value is found to be 0.000669. For higher values, the response of the system displays more oscillations. As the response of the system has no overshoot, this removes the need for a derivative gain K_d thereby resulting in a PI controller. The resulting open loop transfer for the system seen in figure 3.12 with the controller coefficients is found to be

$$H_c(s) = \frac{-2s^2 + 20.62s + 227.46}{17s^3 + 23s^2 + 445.62s + 227.46}. \quad (3.28)$$

Root Locus Analysis with Controller

The root locus analysis is performed again on the system with the identified controller. The equation for the controller is given by equation 3.29.

$$G_c(s) = 0.0001 + \frac{0.000669}{s} \quad (3.29)$$

The root locus plot of the system with the controller can be seen in figure 3.13.

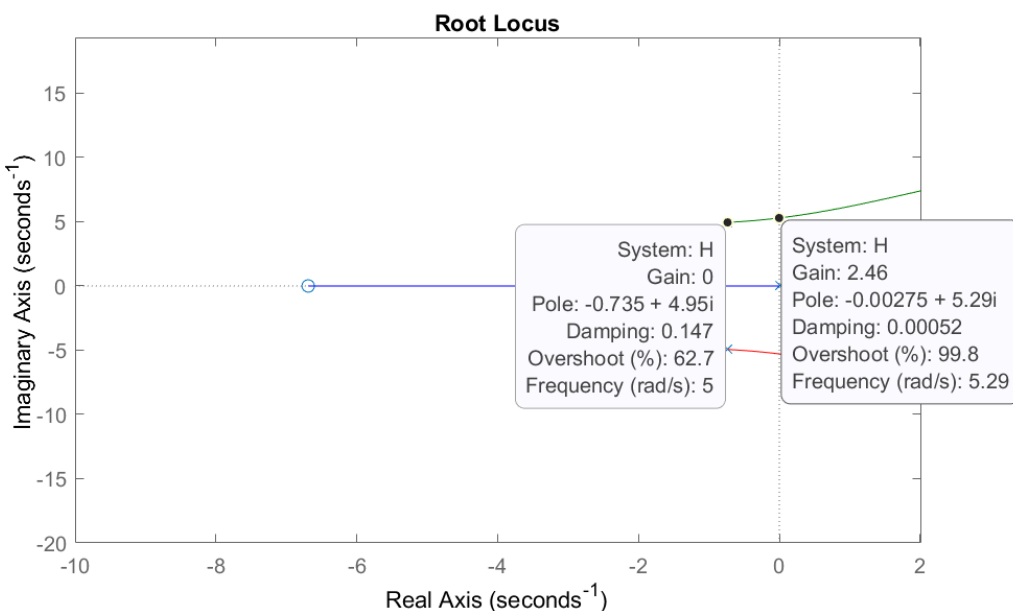


Figure 3.13: Root locus plot of system $H(s)$ with the controller $G_c(s)$ showing the feedback gain values where the system is stable.

The root locus plot 3.13 can be used to identify the feedback gain that can be used to improve the system. In this case, the poles corresponding to the system cannot be moved further to the left with a feedback gain. Therefore, no feedback gain is necessary for the system with the controller.

3.2 Simulation

The models identified for electrolyser, PV and MPPT system and, DC-DC Boost converter in sections 3.1.1, 3.1.2, and 3.1.3 are simulated in MATLAB and Simulink software. The results of the simulation are displayed and discussed in this section.

3.2.1 Simulation of DC-DC Boost Converter Model with Controller

Simulation of transfer function with controller

The transfer function model identified in 3.1.3 is simulated in Simulink. The block diagram of the system and the open loop transfer function can be seen in figure 3.12 and equation 3.28 respectively. The model is simulated over a time period of 50 seconds and the reference is set to 400 V.

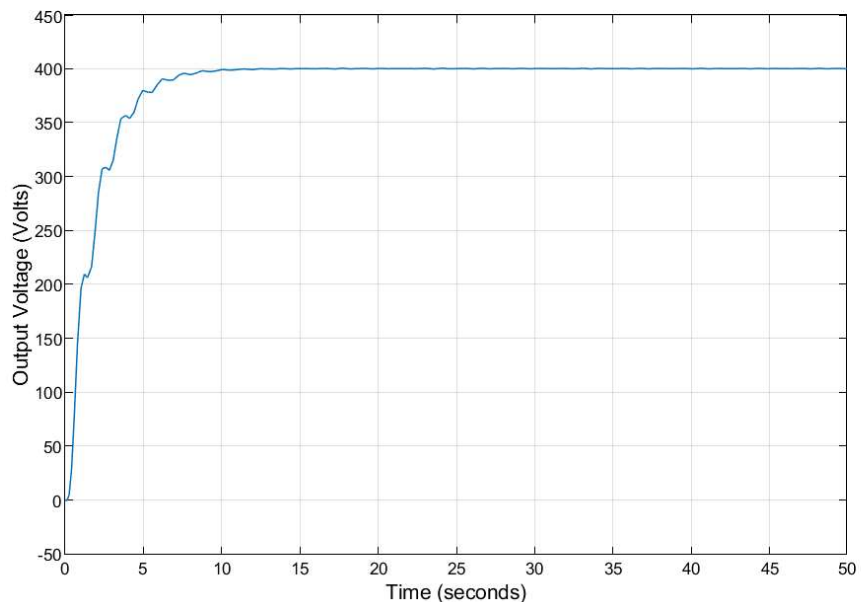


Figure 3.14: Output response of transfer function of DC-DC boost converter with a controller.

Figure 3.14 displays the output of the simulated model. It can be seen that the model converges to a steady state value at around 10 seconds. The output contains some oscillations but no overshoot and the model converges to a final value of 400 V as expected. It can then be concluded that the controller is able to control the output of the transfer function successfully.

Simulation of the DC-DC boost converter circuit with controller

The block diagram of the DC-DC Boost converter in Simulink can be seen in figure 3.15. The converter uses the same specifications and parameters as the transfer function model. The circuit is simulated to see the response of the developed controller.

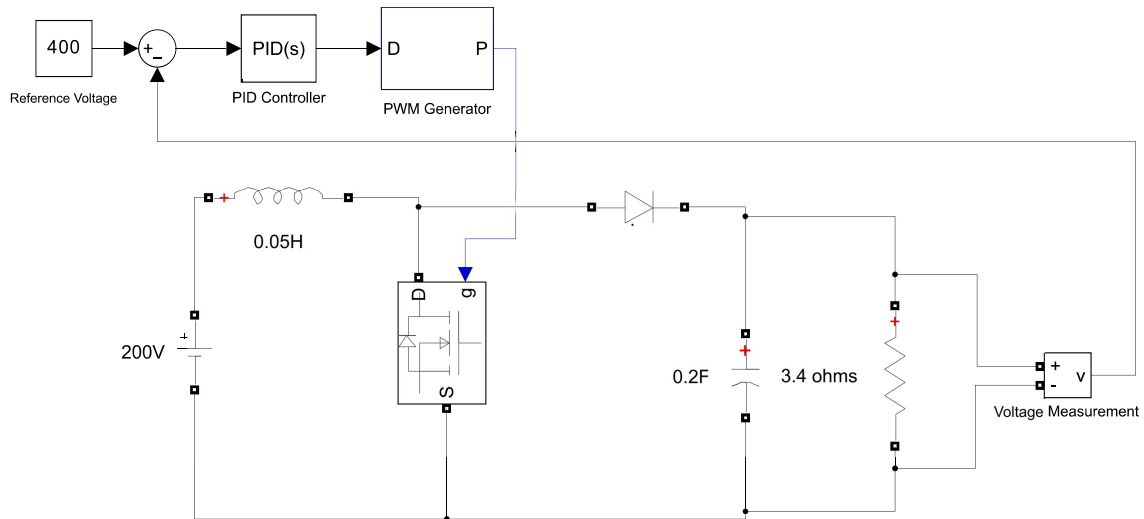


Figure 3.15: Circuit of DC-DC Boost Converter with PID controller on Simulink.

The input voltage is 200 V and the reference voltage is 400 V. The simulation is run for 50 seconds.

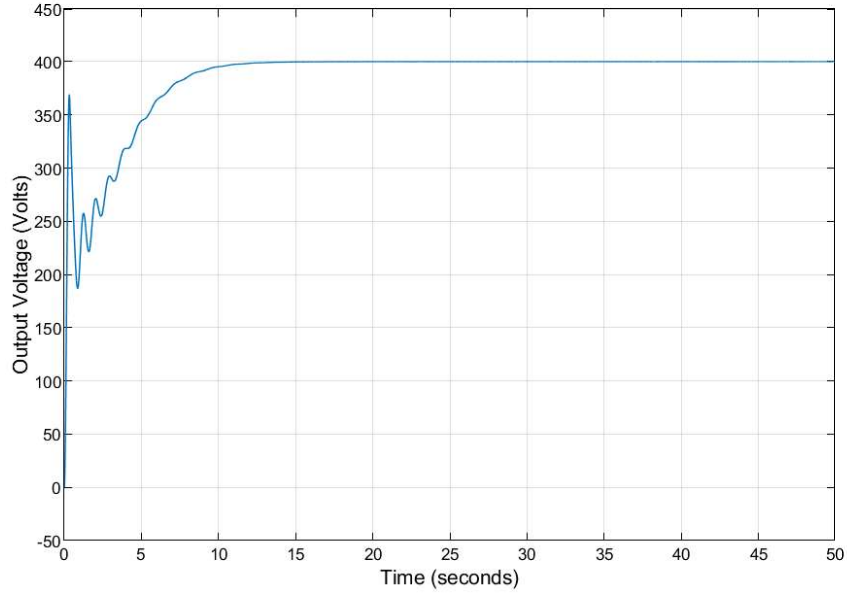


Figure 3.16: Output response of simulated DC-DC boost converter with a controller.

Figure 3.16 shows the output voltage graph of the boost converter. It is seen that the controller is able to stabilize the system successfully in approximately 10 seconds. There is also an inverse response that can be noticed in the graph. The system contains oscillations but no overshoot.

Comparison of transfer function and simulated circuit with a controller

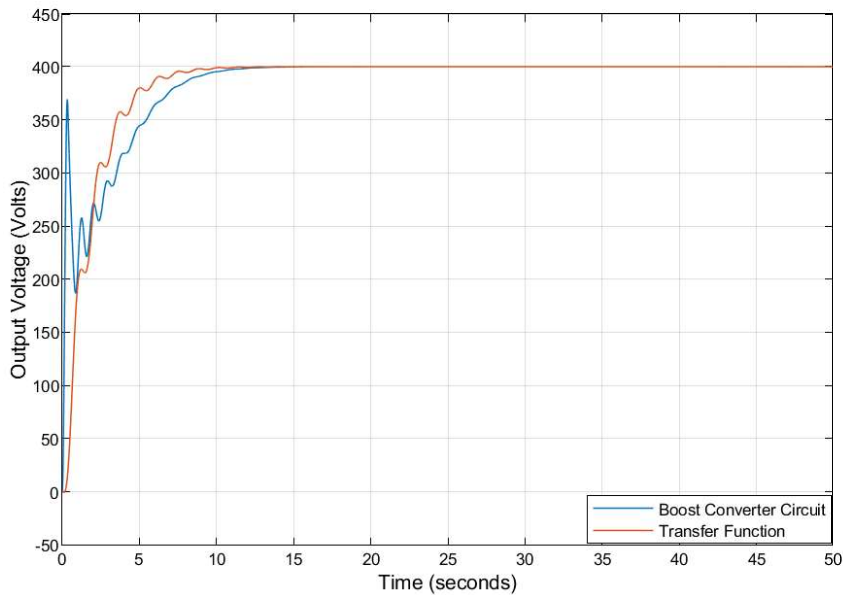


Figure 3.17: Comparison of output responses of transfer function model and simulated circuit model with controllers.

As seen in figure 3.17 the output responses of the transfer function and the simulated boost converter are very similar. The output of the transfer function with controller does not show any inverse response as it does not have any positive zeroes. The simulated boost converter circuit however displays an inverse response. This dynamic of inverse response is not modelled by the transfer function. Both simulations have similar settling times at approximately 10 seconds. Both the simulations are successfully able reach steady state value in less than 15 seconds and the I controller is able to eliminate the steady state error in both cases. It can also be observed that the settling time of the simulated circuit model is slower than the transfer function model by a small amount.

3.2.2 Simulation of PV and MPPT Models

The PV panel used for the simulation is a MATLAB block that features 32 parallel strings and 7 series connected modules per string, resulting in a maximum power output of 213.15 W. Each module contains 60 cells and has an open-circuit voltage of 36.3 V and a short-circuit current of 7.84 A. Irradiance and temperature are parameters which can be changed in the block. At 25 °C it offers the maximum performance. It provides power to the boost converter, and it sends the output value to the MPPT, which receives the voltage and

current from a bus selector and outputs the value of the required duty cycle. The diode I-V curve is calculated using the following equations:

$$I_d = I_0 \left[\exp\left(\frac{V_d}{V_T}\right) - 1 \right], \quad (3.30)$$

$$V_t = \frac{kT}{q} nIN_{cell}. \quad (3.31)$$

Where I_d is the diode current (A), V_d is the diode voltage (V), I_0 is the diode saturation current (A) and nI is the diode ideality factor, which is a number close to 1.0. In the second equation, k is the Boltzman constant, which is $1.3806e^{-23} \text{ JK}^{-1}$. Then, q is the electron charge, with a value of $1.6022e^{-19} \text{ C}$; T is the cell temperature, and finally N_{cell} is the number of cells connected in series in a module. These equations are used to calculate the following curves for the specific PV model:

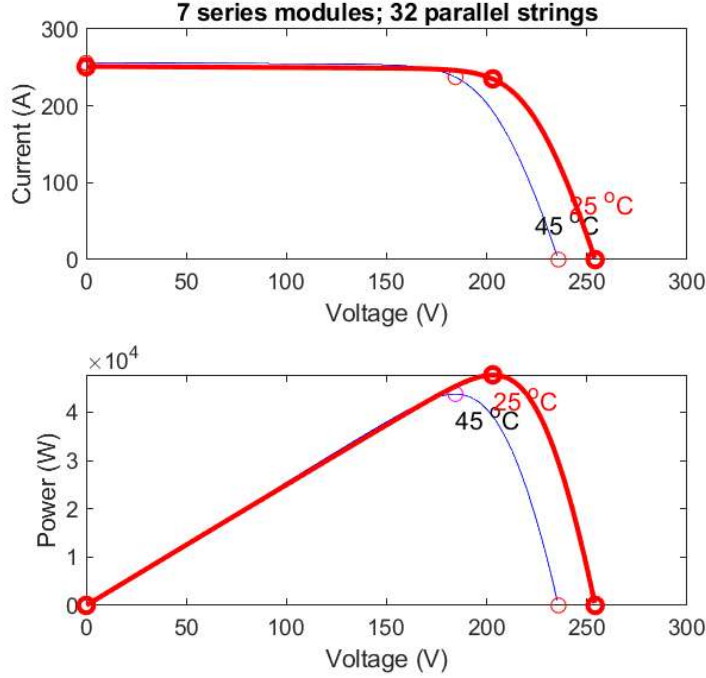


Figure 3.18: IV and PV plots of the PV panel used for the simulation.

At ideal conditions, the panels are able to produce up to $2 * 10^5 \text{ W}$ of power. For the MPPT simulation, the following inputs are set as follow: an irradiance of 1000 W/m^2 and

a temperature of 25 °C.

For simulation of the MPPT, Simulink was also used. The system consists of a function block that receives the voltage and current values from the PV panel and outputs the duty cycle D. That value is then converted to a PWM signal and sent directly to the boost converter switch. The boost converter is the same as in figure 3.15. The script used in the function block is included in appendix B. The system looks as follows:

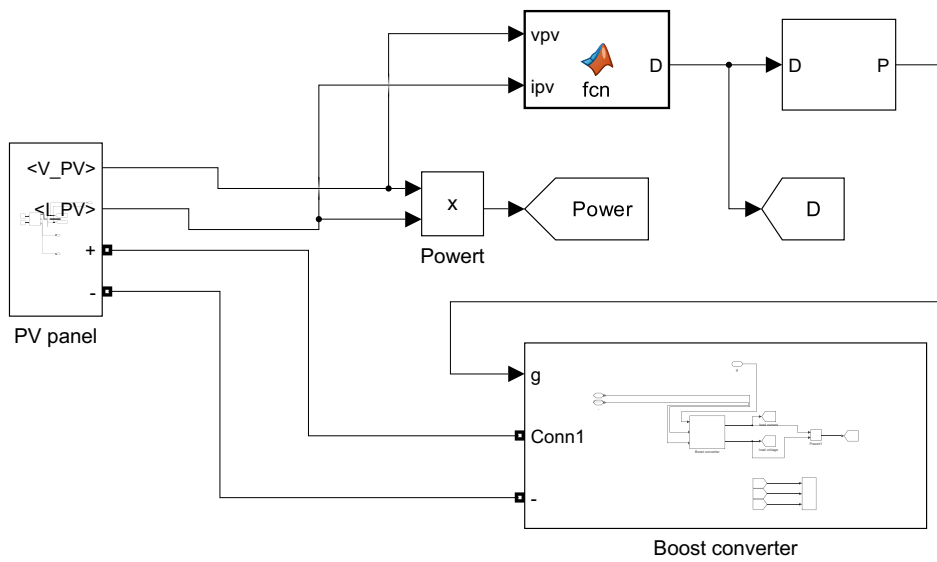


Figure 3.19: Simulink model used for the MPPT simulation.

The output voltage, power and duty cycle can be seen in figure 3.20

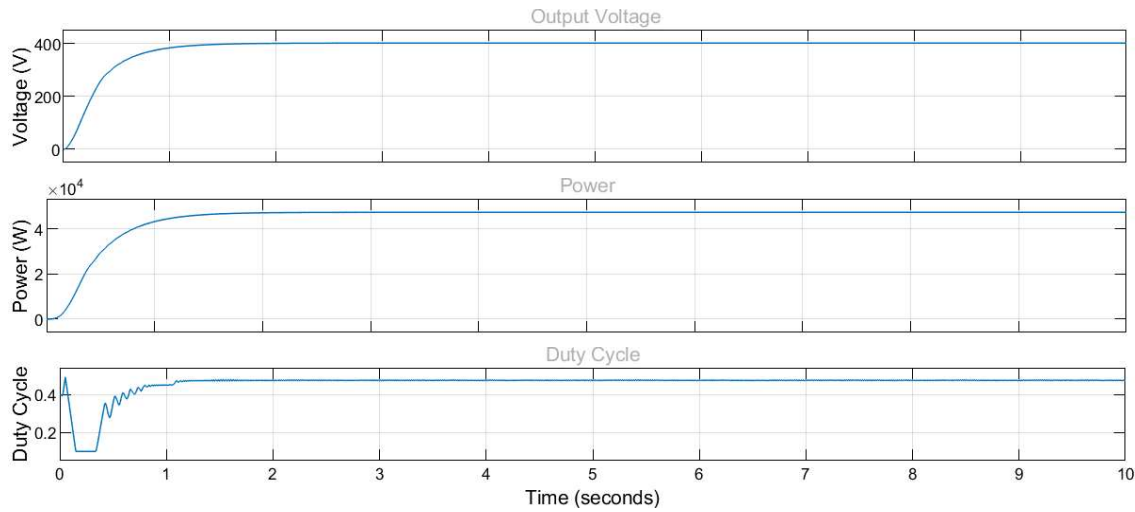


Figure 3.20: Output of the scope from the model in figure 3.19.

All values converge to a fixed value, where the MPP should be according to the design. The duty cycle corresponding to this was 0.4761. To verify this, tests comparing power to duty cycles from 0 to 1 were performed, and the results gathered in table 3.1:

Table 3.1: A table comparing duty cycles to power output for the PV-boost converter simulation.

Duty Cycle	0	0.1	0.2	0.3	0.4	0.476	0.5	0.6	0.7	0.8	0.9	1.0
Power(kW)	16.6	20.6	26.0	33.0	41.4	47.4	47.1	32.4	18.1	7.89	1.82	0.000060

The gathered data shows that the algorithm was able to find the MPP.

3.2.3 Integrated Model

As can be seen in figure 3.21, this is the Simulink file of the integrated model. This file includes an MPPT algorithm and a PID controller and is able to switch between both modes thanks to the switch located before the PWM generator. The scope on the top plots the input values while the one below plots the output ones.

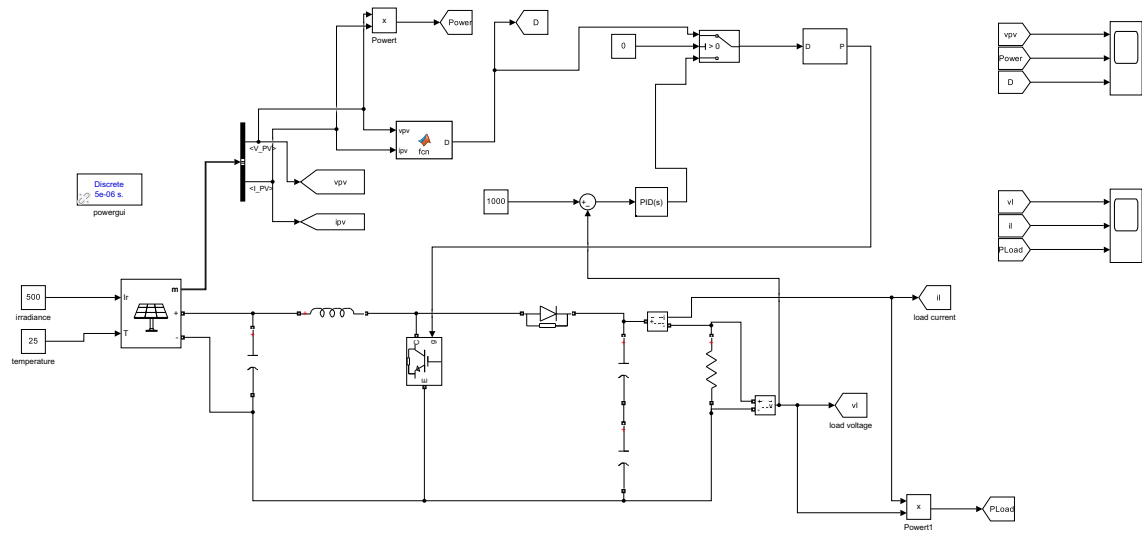


Figure 3.21: Simulink model of the integrated system.

Chapter 4

Testing and Validation

4.1 Implementation

The physical implementation was built similarly to the simulation, with some additions and simplifications. The electrical model of the electrolyser was not implemented as in the simulation, as high currents were not desirable or feasible to work with. A higher load of $300\ \Omega$ was used, and the reversible voltage was not implemented, as it would not fit with the high load and low voltages produced in lab. The lower bound of the systems operating envelope was set at 10 V. It was found during testing that the upper limit the current sensor could operate in was 15 V, see section 4.1.2. Voltage measurements could, however, be performed above 15 V and tests were performed above 15 V, see section 4.2.

All code to read measurements, output a PWM signal and run the MPPT algorithm was run on an Arduino Uno. In order to provide data on the voltage and current of the circuit, voltage dividers and a current sensor were built.

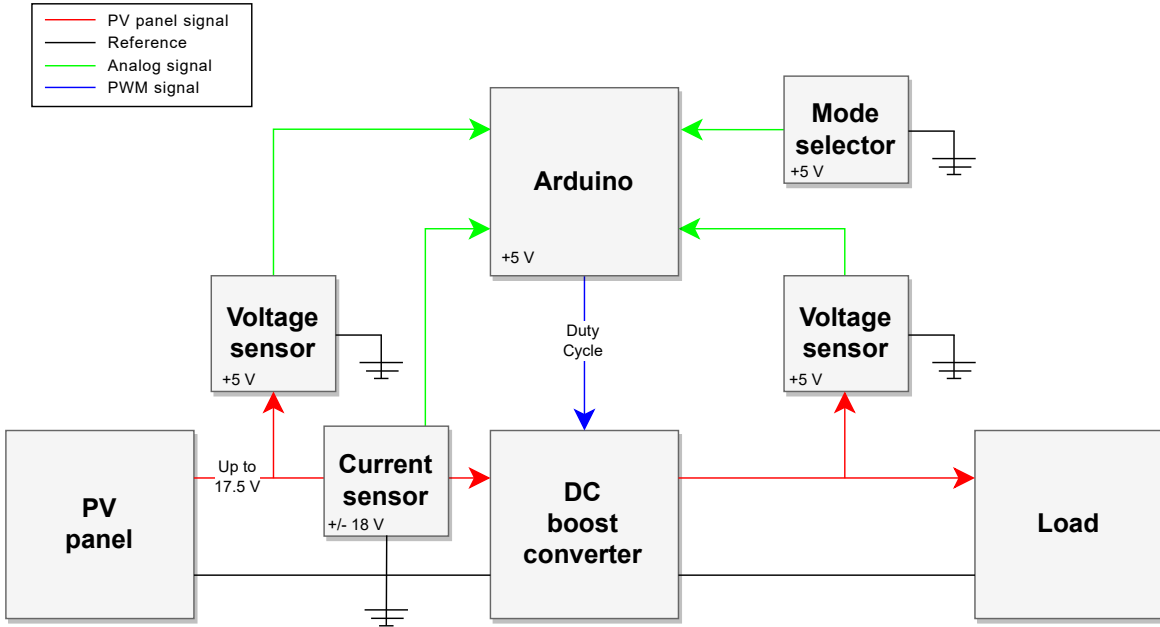


Figure 4.1: Block diagram

4.1.1 Microcontroller

The board chosen is an Arduino Uno, based on the ATmega328P chip [46]. It has sufficient processing capabilities for the purpose, can drive the duty cycle of the boost converter with one of its PWM pins, and can sample the analog signals from the sensors with its 10 bit ADC (Analog-to-digital converter). Furthermore, a PID control library is available, which allows to tune the controller directly on the microcontroller [47].

4.1.2 Sensors

Voltage measurements were made at the panel output and converter output using voltage dividers. At the input $100k\ \Omega$ and $470k\ \Omega$ resistors were used, and at the output $20k\ \Omega$ and $2.2k\ \Omega$.

The current sensor, shown in figure 4.2, is constructed using the principle of voltage drop over a shunt resistor. An instrumentation amplifier was used to multiply the voltage drop across the shunt instead of the more commonly used operational amplifier, to avoid issues related to high-side current measurements. When using operational amplifiers, a differential configuration is required for high-side measuring and the precision of the readings suffer due to the common-mode partial amplification. This problem is due to the

relatively low Common-Mode Rejection Ratio (CMRR) of operational amplifiers, as well as to the need for precisely matched resistors. In comparison the instrumentation amplifier includes internal laser-trimmed resistor which reduces notably the issue.

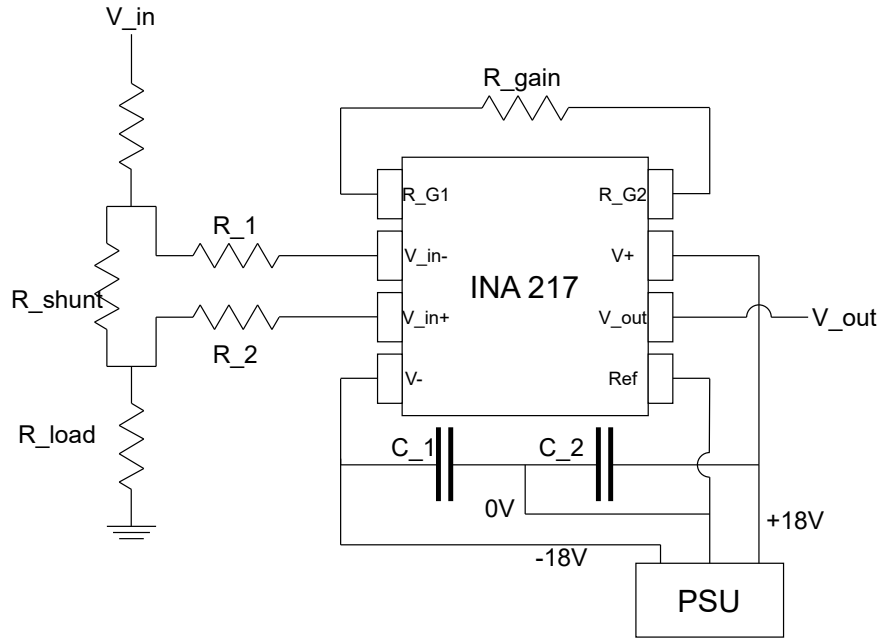


Figure 4.2: Current Sensor circuit

The maximum input voltage at which the amplifier could operate was at 15 V, which was tested in the lab. In addition to this, working at up to 15 V only worked up to a certain amplification, which was around 370. This corresponding to $R_G = 27 \Omega$ as per manufacturer data sheet gain calculation [48]. After this value of gain the operating range rapidly decreased. The capacitors values were set at $0.1 \mu\text{F}$ as per manufacturer specifications, and the resistors R_1 and R_2 were experimentally tested for function, and both set at 100Ω . Testing the current sensor was done in the operating range, resulting in the following table:

Table 4.1: Current sensor readings comparison with supply

Input Voltage (V)	Supply Current (mA)	Arduino Measurement (mA)
10	34	29.85
11	38	32.94
12	41	35.93
13	45	39.02
14	48	42.01
15	52	45.11

Taking the average of the percentage difference, a constant was implemented in the code to correct for this deviation, $currentError = 1.1473$.

4.1.3 Boost Converter

As the possibility to control the duty cycle is essential for the testing, the boost converter is built on the breadboard. Suitable components for the circuit requirements are chosen based on their availability in the laboratory.

- MOSFET: N-Channel IRLZ44N

Features, high switching speeds and its low resistance while in ON state.

- Diode: HER105 943

This component has a fast recovery time, which can handle the fast switching of the MOSFET and minimizes switching losses, improving the overall circuit efficiency.

- Inductor: 470 μ H

- Capacitor: 220 μ F 63 V

The capacitor and inductor values were chosen due to availability in the laboratory.

4.1.4 Panel

The panel used was a mono-crystalline silicon PV module with a maximum power of 50W (+/- 3 %). The choice of panel done after the usage in real applications, as crystalline panels are widely used in industrial solar installations [49]. The voltage at maximum power point of the panel is 17.5 V, therefore the the circuit is required to be able to perform at that potential.

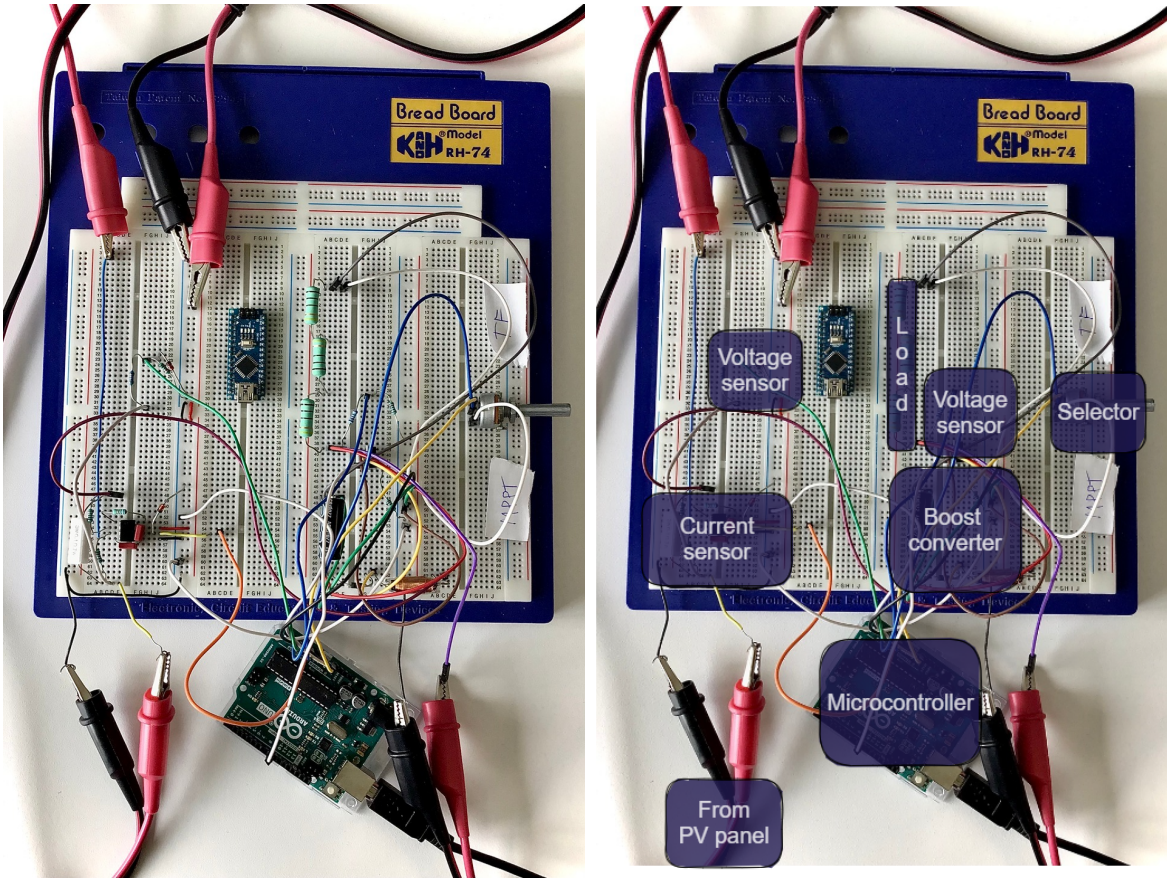


Figure 4.3: Experiment setup on a breadboard

4.2 Experiments

With the sensors, boost converter, and microcontroller implemented in the breadboard, the setup can be tested and evaluated through a series of experiments.

4.2.1 PI Controller with a Power Supply

The aim of this experiment was to verify that the voltage regulation mode of the system would boost the voltage of the output to 24 V during a changing input voltage.

Method

A feedback loop is added to the boost controller. The output voltage is read through a voltage divider with $20K\ \Omega$ and $2.2K\ \Omega$ resistors. The output is then subtracted to the setpoint which in this case is 24 V. The experiment is run for voltages between 10 V and 15 V where the voltage is slowly increased from 10 V to 15 V. The PI controller is set up in the Arduino code to control the output voltage. Due to the change in parameters of the boost converter and the input and output specifications, a different PI controller is used. The proportional gain and the integral gain are found through the Ziegler-Nichols method of tuning.

Results

Through the Ziegler-Nichols tuning method, the gains for the PI controller are identified. The proportional gain $K_p=0.0135$ and the integral gain $K_i=0.09$ are used in the PI controller. The input current, input voltage, duty cycle and output voltage are recorded and plotted. The input current can be seen in figure 4.4.

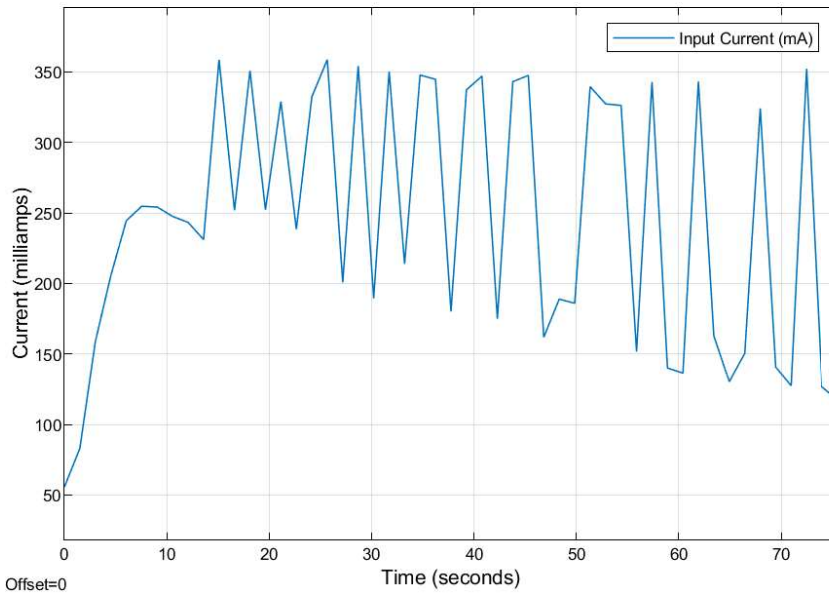


Figure 4.4: Plot of the input currents for the voltage regulation mode experiment.

The large fluctuations are likely due to inaccuracy of the current sensor. The input voltage and output voltage can be seen in figure 4.5. It can be seen that the controller is able to stabilize the output voltage close to 24 V for varying input voltages.

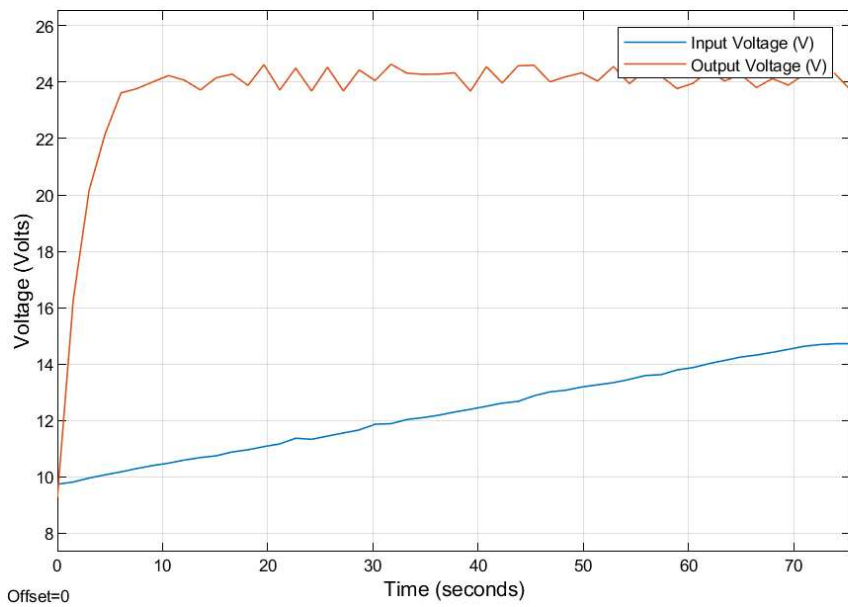


Figure 4.5: Plot of the input and output voltages for the voltage regulation mode experiment.

The duty cycle observed in the figure 4.6 also shows the relationship between the input and output voltages.

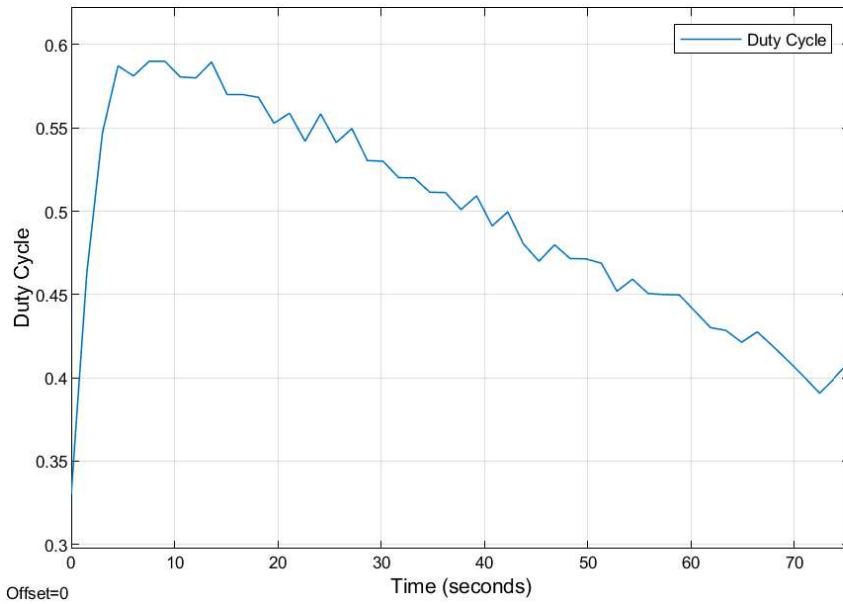


Figure 4.6: Plot of the duty cycles for the voltage regulation mode experiment.

The test thus shows that the voltage is successfully regulated to around 24 V output, and that for a rising input voltage, the duty cycle falls.

4.2.2 MPPT and PI Controllers with a PV Panel

The aim of this experiment is to observe the behaviour of both systems: the one with the MPPT algorithm and PI controller under different conditions.

Method

On a day with favourable solar irradiance, meaning that the panel output surpasses the minimum voltage for the system to work, the panel is connected to the setup. Necessary adjustments to the system parameters are made. Voltage, current, and duty cycle data is recorded.

Results

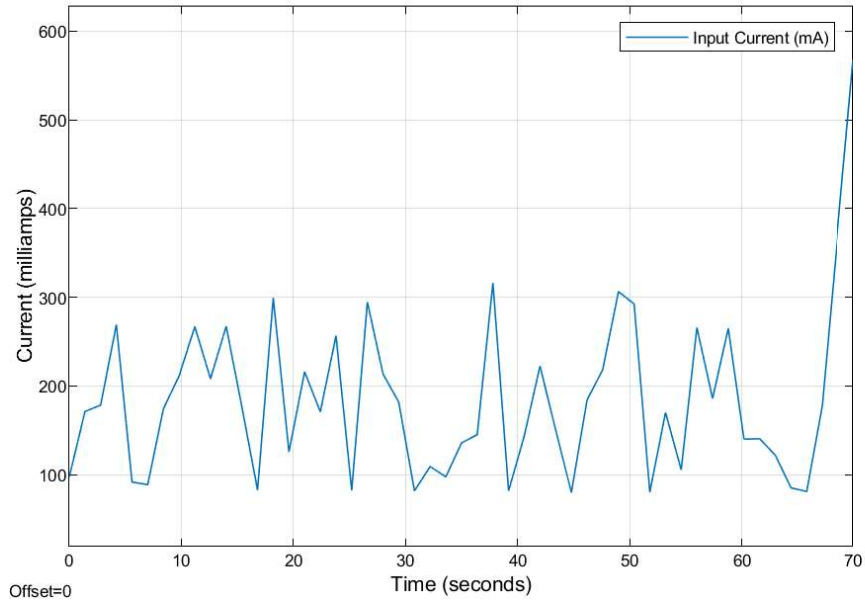


Figure 4.7: Plot of the input currents for the MPPT mode in the panel.

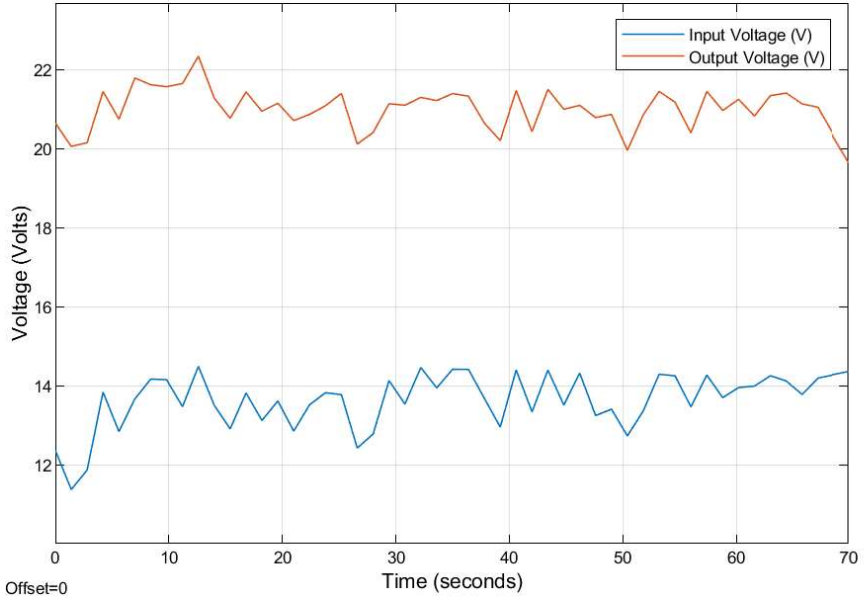


Figure 4.8: Plot of the input and output voltages for the MPPT mode in the panel.

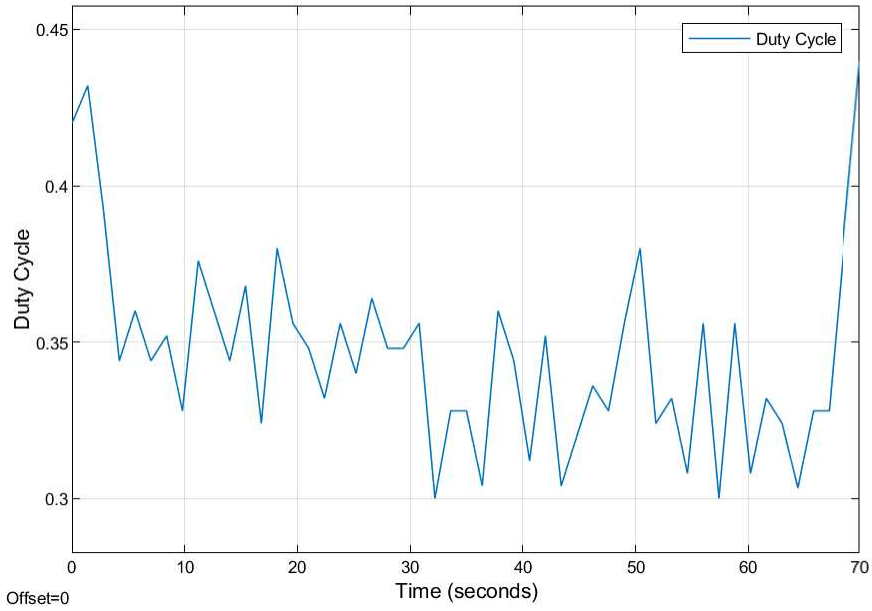


Figure 4.9: Plot of the duty cycles for the MPPT mode in the panel.

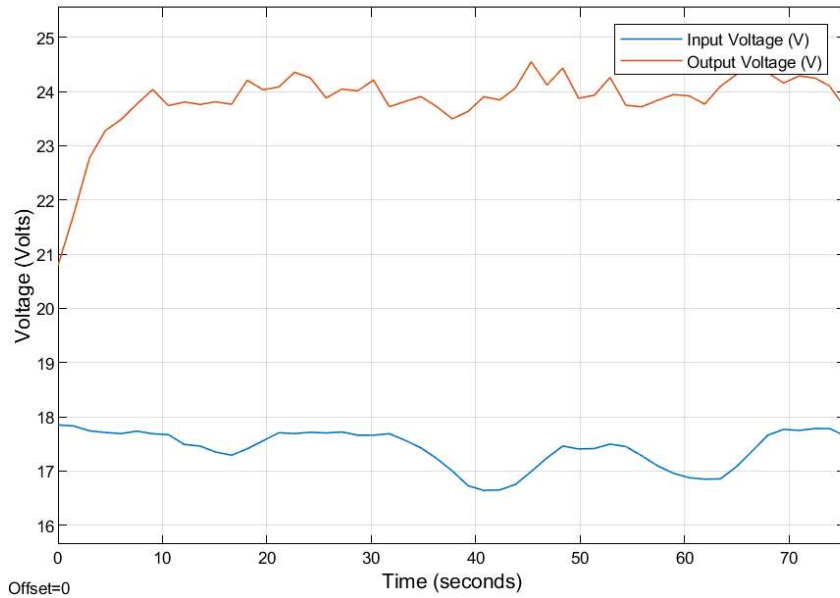


Figure 4.10: Plot of the input and output voltages for the voltage regulation mode in the panel.

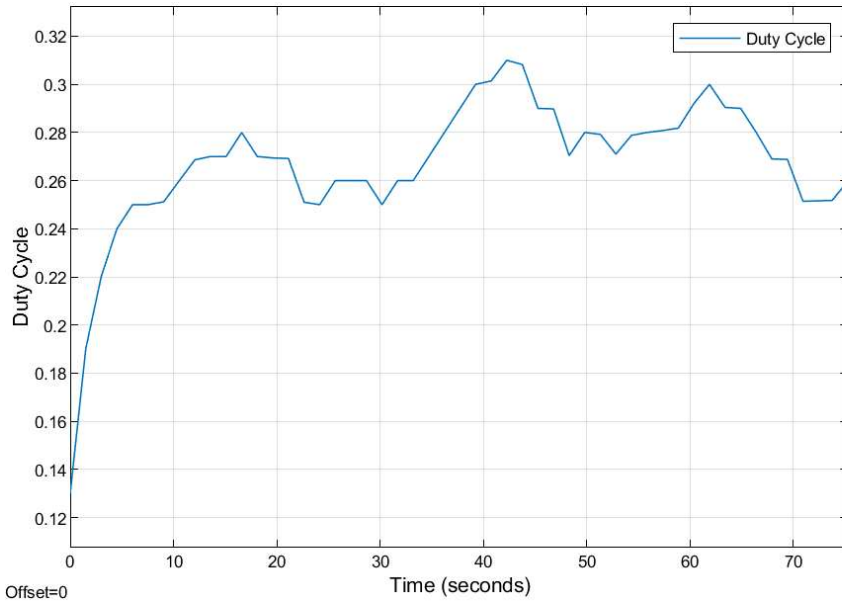


Figure 4.11: Plot of the input and output voltages for the voltage regulation mode in the panel.

From the plots it can be seen that the PI controller successfully regulates the voltage to the setpoint. The MPPT does seem to hover around a certain voltage value, however the current and duty cycle fluctuate significantly, and it is difficult to determine anything from these tests. Changing irradiance may be an additional factor causing the fluctuations.

4.2.3 MPPT accuracy

The aim of this test is to determine whether the duty cycle calculated by the MPPT algorithm is correct.

Method

First, with the PV panel connected to the setup, the code in MPPT mode is executed, and duty cycle found by the software noted. Subsequently and under similar irradiance conditions, a code that increments the duty cycle from 0 to 1 in 0.1 steps is executed. Current and voltage data from the panel are extracted both from the Arduino sensors and from laboratory multimeters.

Results

When running the Arduino on MPPT mode, the algorithm set the duty cycle at 0.1. Next, when the sweeping through all the duty cycle values, the multimeter data show the MPP in fact has to be at 0.1, while the data extracted from the Arduino sensors show the MPP at a 0.3 duty cycle. This means that either the MPPT fails to calculate the correct duty cycle or there are irradiance changes in the lapse between tests.

Table 4.2: PV panel V and I readings for duty cycles ranging 0 to 1.

Duty cycle	Multimeter			Arduino		
	V in (V)	I in (mA)	P in (mW)	V in (V)	I in (mA)	P in (mW)
0	14.43	46	663.78	14.18	45.13	639.94
0.1	13.17	53.29	701.83	12.88	63.35	815.95
0.2	11.57	58.65	678.58	11.39	84.30	960.18
0.3	7.48	64.89	485.38	9.47	106.18	1005.52
0.4	7.44	67.35	501.08	7.49	113.94	853.41
0.5	5.43	70.32	381.84	5.49	95.84	526.16
0.6	3.76	73.23	275.34	3.49	55.16	192.51
0.7	2.28	74.8	170.54	2.17	73.75	160.04
0.8	1.21	75.88	91.81	1.08	77.40	83.59
0.9	0.5	76.56	38.28	0.40	75.04	30.02
1	0.23	75.57	17.38	0.12	74.70	8.96

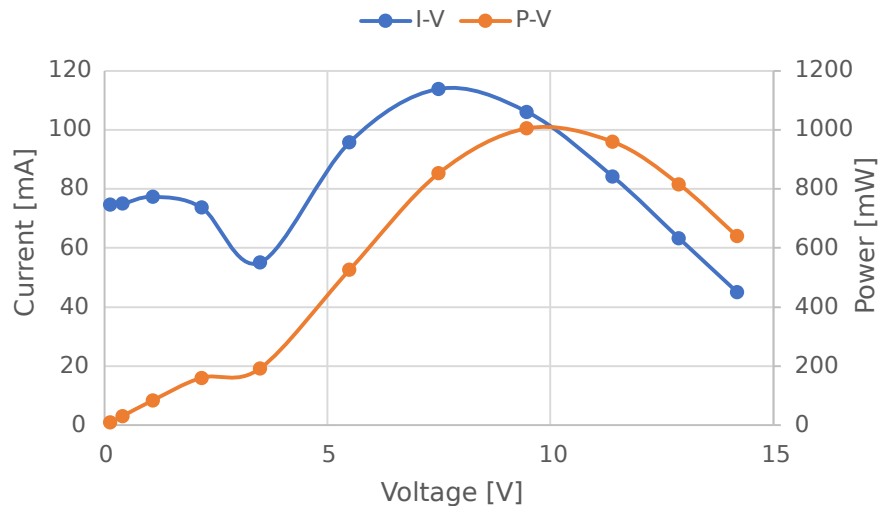


Figure 4.12: Arduino readings I-V and P-V curves for duty cycles ranging 0 to 1.

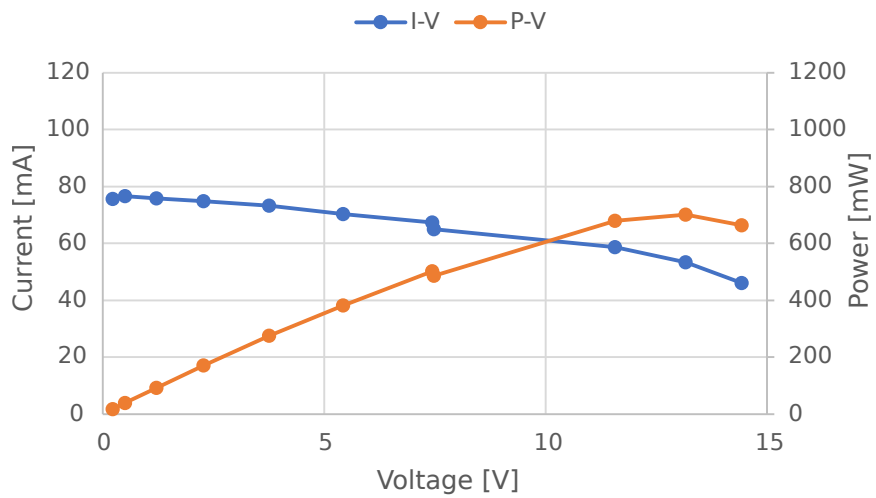


Figure 4.13: Multimeter readings I-V and P-V curves for duty cycles ranging 0 to 1.

Chapter 5

Discussion and Conclusion

5.1 Discussion

Models were developed using an analytical approach. After an initial research phase, models for the PV, MPPT, boost converter, and electrolyser were derived from the existing literature. Although, the full electrolyser model was not utilised, for future implementations and improvements the work done for this project is an important step.

The simulation, which was created for both the PI and MPPT control system, worked as intended. The PI controller managed to boost the voltage up to 400 V, and the MPPT system algorithm found the MPP voltage level. The PI controller reached the target voltage in approximately 10 seconds, while the MPPT did it in approximately 1 second. Thus, the implementation of the MPPT algorithm as it is could potentially achieve slightly higher production due to lower settling times, if the input voltage varies greatly. Furthermore, some simulation with different capacitor and inductor values did show that circuit characteristics can be changed with different values, however it was decided not to be a system parameter that would be changed.

When the circuit was implemented in the breadboard, the obtained plots of the conducted tests showed that the PI system is able to quickly compute the duty cycle that the boost converter uses to modify the output voltage. When the PV panel is used as an input, it can be seen that the input voltage is not stable and both the MPPT and PI systems are able to regulate the output voltage, but not being as stable as using a laboratory power supply as the source of input voltage. For the MPPT system however it is difficult to say whether it worked in practice, due to fluctuating and poor current measurements, though it did keep the voltage output quite stable. Further tuning of the software, hardware parameters and testing in a wider range of weather conditions could be done to improve performance.

The component availability sets the input upper boundary to 15 V, as the current sensor used has a limitation of only reading the current when the voltage at the input was under 15 V. This explains the lack of an input current plot for the PI system as the current sensor was unable to read the input current. The boundaries set also made it unfeasible to do a hydrogen production physical test, as the reversible voltage for the load surpasses the working voltages.

5.2 Conclusion

Development of the project has led to some important milestones, as well as highlighting key issues which would necessitate further research. A large focus of the project has been on the theory and application of control theory, including modelling of physical systems, simulation of models, and implementing linear control techniques. The work done on developing a PI controller and an MPPT algorithm has meant that the group was able to perform comparisons on the ability to boost and stabilize voltage in two different manners. Time restrictions meant that some simplifications of the system were necessary, such as not physically utilising the electrical equivalent circuit and using this to compare theoretically derived hydrogen yields. Issues such as sensor limitations could also feasibly have been solved given more time. The initiating problem for the project was:

Can renewable energy be utilized efficiently for PtX applications, and can this be improved to become economically beneficial?

It can be concluded that although practical tests proving this statement were not made, the technical framework built in the course of the project can quite surely be used to delve into both efficiency and, in later stages, economic aspects of the PtX field.

Bibliography

- [1] Gero Rueter. *Power-to-X: Clean energy to replace oil and gas*. Dec. 2019. URL: <https://www.dw.com/en/power-to-x-the-secret-to-a-100-renewable-energy-system/a-51662014>.
- [2] *Power to X*. Feb. 2023. URL: <https://europeanenergy.com/green-solutions/power-to-x/>.
- [3] Energy Danish Ministry of Climate and Utilities. *The Governments strategy for POWER TO X*. 2021. URL: https://ens.dk/sites/ens.dk/files/ptx/strategy_ptx.pdf.
- [4] Björn Bofinger. *What are Power to X solutions?* 2022. URL: <https://as-schneider.blog/2022/03/02/what-are-power-to-x-solutions/>.
- [5] European Comission. *REPowerEU: affordable, secure and sustainable energy for Europe*. 2022. URL: https://commission.europa.eu/strategy-and-policy/priorities-2019-2024/european-green-deal/repowereu-affordable-secure-and-sustainable-energy-europe_en.
- [6] Paul Denholm and Trieu Mai. "Timescales of energy storage needed for reducing renewable energy curtailment". In: *Renewable Energy* 130 (2019), pp. 388–399.
- [7] Vattenfall. *Electricity as an enabler*. URL: <https://group.vattenfall.com/what-we-do/roadmap-to-fossil-freedom/electricity-as-an-enabler/direct-and-indirect-electrification>.
- [8] International Energy Agency. *The Future of Hydrogen*. 2019. URL: <https://www.iea.org/reports/the-future-of-hydrogen>.
- [9] National Grid. *The hydrogen colour spectrum*. URL: <https://www.nationalgrid.com/stories/energy-explained/hydrogen-colour-spectrum>.
- [10] H2 Energy. *Major green hydrogen power-to-X-facility planned in Esbjerg*. 2021. URL: <https://h2energy.ch/en/2021/09/23/major-green-hydrogenpower-to-x-facility-planned-in-esbjerg/>.
- [11] Adriaan Paets van Troostwijk and Johan Rudolph Deiman. In: *Algemeen magazijn, van Wetenschap, Konst en Smaak* 4 (1790), p. 909.

- [12] R de Levie. "The electrolysis of water". In: *Journal of Electroanalytical Chemistry* 476.1 (1999), pp. 92–93. ISSN: 1572-6657. DOI: [https://doi.org/10.1016/S0022-0728\(99\)00365-4](https://doi.org/10.1016/S0022-0728(99)00365-4). URL: <https://www.sciencedirect.com/science/article/pii/S0022072899003654>.
- [13] William Nicholson and Anthony Carlisle. "Experiments with a new electrical or galvanic apparatus". In: *Journal of Natural Philosophy, Chemistry the Arts* 4 (1801), pp. 179–187. URL: <https://www.biodiversitylibrary.org/item/20168>.
- [14] W.H. Pauling Linus;Freeman and Co. *General Chemistry*. Elsevier B.V, San Francisco, 1971.
- [15] *Water electrolysis – a promising remedy for the off-grid solar energy storage problem*. URL: <https://cordis.europa.eu/article/id/418019-water-electrolysis-a-promising-remedy-for-the-off-grid-solar-energy-storage-problem>.
- [16] Daojin Zhou et al. "Recent Advances in Non-Precious Metal-Based Electrodes for Alkaline Water Electrolysis". In: *ChemNanoMat* 6.3 (2020), pp. 336–355. DOI: <https://doi.org/10.1002/cnma.202000010>. URL: <https://onlinelibrary.wiley.com/doi/abs/10.1002/cnma.202000010>.
- [17] Yakdehige De Silva and Peter Middleton. "Design of an Alkaline Electrolysis Stack". PhD thesis. 2017, pp. 17–25. DOI: [10.13140/RG.2.2.14351.12964](https://doi.org/10.13140/RG.2.2.14351.12964).
- [18] Marcelo Carmo et al. "A comprehensive review on PEM water electrolysis". In: *International Journal of Hydrogen Energy* 38.12 (2013), pp. 4901–4934. ISSN: 0360-3199. DOI: <https://doi.org/10.1016/j.ijhydene.2013.01.151>. URL: <https://www.sciencedirect.com/science/article/pii/S0360319913002607>.
- [19] Yujing Guo et al. "Comparison between hydrogen production by alkaline water electrolysis and hydrogen production by PEM electrolysis". In: *IOP Conference Series: Earth and Environmental Science* 371.4 (2019), p. 2. DOI: [10.1088/1755-1315/371/4/042022](https://doi.org/10.1088/1755-1315/371/4/042022). URL: <https://dx.doi.org/10.1088/1755-1315/371/4/042022>.
- [20] Yi Sun et al. "Solid oxide electrolysis cell under real fluctuating power supply with a focus on thermal stress analysis". In: *Energy* 261 (2022), p. 3. ISSN: 0360-5442. DOI: <https://doi.org/10.1016/j.energy.2022.125096>. URL: <https://www.sciencedirect.com/science/article/pii/S0360544222019910>.
- [21] B. Yildiz. "6 - Reversible solid oxide electrolytic cells for large-scale energy storage: challenges and opportunities". In: *Functional Materials for Sustainable Energy Applications*. Ed. by John A. Kilner et al. Woodhead Publishing Series in Energy. Woodhead Publishing, 2012, 149–179e. ISBN: 978-0-85709-059-1. DOI: <https://doi.org/10.1533/9780857096371.2.147>. URL: <https://www.sciencedirect.com/science/article/pii/B9780857090591500063>.
- [22] Manuel Götz et al. "Renewable Power-to-Gas: A technological and economic review". In: *Renewable Energy* 85 (2016), p. 1373. DOI: [10.1016/j.renene.2015.07.066](https://doi.org/10.1016/j.renene.2015.07.066).

- [23] International Energy Agency. "Renewable Energy Market Update". In: (2022). URL: <https://www.iea.org/reports/renewable-energy-market-update-may-2022>.
- [24] Electrical Academia. "Maximum Power Point Tracking (MPPT) Charge Controller Working Principle". In: (2018). URL: <https://electricalacademia.com/renewable-energy/maximum-power-point-tracking-mppt-charge-controller-working-principle/>.
- [25] Hittite Journal of Science and Engineering. "A Review and Classification of Most Used MPPT Algorithms for Photovoltaic Systems". In: (2021). URL: <https://dergipark.org.tr/tr/download/article-file/1609909>.
- [26] Abdelaziz El Ghzizal Saad Motahhir Aboubakr El Hammoumi. "The most used MPPT algorithms: Review and the suitable low-cost embedded board for each algorithm". In: (2020). URL: https://www.sciencedirect.com/science/article/pii/S0959652619338533?casa_token=RTGkswrv4EYAAAAA:ByAg-0qeksr1kqJtmD2dh2LhPMyiDB1TOYqA1x4iwiF2ZtKjpPSEEUSCU7L-w.
- [27] S. Saon T. Tuwoso Hakkun Elmunsyah S. W. Mudjanarko A. S. Mahdi A. K. Mhamad. "Maximum power point tracking using perturb and observe, fuzzy logic and ANFIS". In: (2020). URL: <https://link.springer.com/article/10.1007/s42452-019-1886-1>.
- [28] American Journal of Engineering Research (AJER). "Comparative Study of PO and InC MPPT Algorithms". In: (2013). URL: [https://www.ajer.org/papers/v2\(12\)/ZT212402408.pdf](https://www.ajer.org/papers/v2(12)/ZT212402408.pdf).
- [29] Amjad Ali et al. "Review of Online and Soft Computing Maximum Power Point Tracking Techniques under Non-Uniform Solar Irradiation Conditions". In: *Energies* 13.12 (2020). ISSN: 1996-1073. DOI: 10.3390/en13123256. URL: <https://www.mdpi.com/1996-1073/13/12/3256>.
- [30] Jae-Sub Ko, Jun-Ho Huh, and Jong-Chan Kim. "Overview of Maximum Power Point Tracking Methods for PV System in Micro Grid". In: *Electronics* 9.5 (2020). ISSN: 2079-9292. DOI: 10.3390/electronics9050816. URL: <https://www.mdpi.com/2079-9292/9/5/816>.
- [31] Mohamed Abdullrahman Alranini Zakaria Mohamed Salem Elbarbary. "Review of maximum power point tracking algorithms of PV system". In: (2021). URL: <https://www.emerald.com/insight/content/doi/10.1108/FEBE-03-2021-0019/full/html>.
- [32] Timur Yuldashev and Andrey Solovev. *DC-to-DC Converters: Functions, Common Types Design Principles, Applications, and Challenges*. Nov. 2022. URL: <https://www.integrasources.com/blog/dc-dc-converters-functions-types-design-applications-challenges/>.
- [33] Electrical Technology and Electrical Technology. *Buck Converter 8211; Circuit, Design, Operation and Examples*. Sept. 2022. URL: <https://www.electricaltechnology.org/2020/09/buck-converter.html>.

- [34] Basanta Subedi. *Boost Converter: Basics, Working, Design 038; Application*. Oct. 2022. URL: <https://how2electronics.com/boost-converter-basics-working-design-application/>.
- [35] Electronics Mind. *Buck-Boost Converter - Circuit Diagram, Working amp; Applications*. Sept. 2022. URL: <https://www.electronicsmind.com/buck-boost-converter/>.
- [36] Jarosław Milewski et al. "Hydrogen production in solid oxide electrolyzers coupled with nuclear reactors". In: *International Journal of Hydrogen Energy* 46.72 (2021). Special Issue on HYPOTHESIS XV, pp. 35765–35776. ISSN: 0360-3199. DOI: <https://doi.org/10.1016/j.ijhydene.2020.11.217>. URL: <https://www.sciencedirect.com/science/article/pii/S0360319920344670>.
- [37] Yi Sun et al. "Multi-objective optimizations of solid oxide co-electrolysis with intermittent renewable power supply via multi-physics simulation and deep learning strategy". In: *Energy Conversion and Management* 258 (2022), p. 115560. ISSN: 0196-8904. DOI: <https://doi.org/10.1016/j.enconman.2022.115560>. URL: <https://www.sciencedirect.com/science/article/pii/S0196890422003569>.
- [38] *Hydrogen from renewable power: Technology outlook for the energy transition*. 2018. URL: <https://www.irena.org/publications/2018/Sep/Hydrogen-from-renewable-power>.
- [39] Alexander Buttler and Hartmut Spliethoff. "Current status of water electrolysis for energy storage, grid balancing and sector coupling via power-to-gas and power-to-liquids: A review". In: *Renewable and Sustainable Energy Reviews* 82 (2018), pp. 2440–2454. ISSN: 1364-0321. DOI: <https://doi.org/10.1016/j.rser.2017.09.003>. URL: <https://www.sciencedirect.com/science/article/pii/S136403211731242X>.
- [40] Slobodan Petrovic. *Electrochemical energy storage*. McGraw-Hill, New York, 2022, p. 175. ISBN: 9781260012002.
- [41] Øystein Ulleberg. "Modeling of advanced alkaline electrolyzers: A system simulation approach". In: *International Journal of Hydrogen Energy* 28 (2003), p. 25. doi: 10.1016/S0360-3199(02)00033-2.
- [42] David Martinez and Ramon Zamora. "MATLAB Simscape Model of An Alkaline Electrolyser and Its Simulation with A Directly Coupled PV Module". In: *INTERNATIONAL JOURNAL OF RENEWABLE ENERGY RESEARCH* 8 (2018).
- [43] Robert W.Erickson and Dragan Maksimovic. *Fundamentals of Power Electronics. Second Edition*. Secaucus, NJ, USA: Kluwer Academic Publishers, 2000.
- [44] Frederik Dostal. *Upper End Limitations of a Duty Cycle*. URL: <https://www.analog.com/en/technical-articles/upper-end-limits-duty-cycle>.
- [45] Wei Xi. *Modeling and Control of dc/dc Boost Converter in FC systems*. URL: <http://www-personal.umich.edu/~annastef/FuelCellPdf/problemboostconverter.pdf>.

- [46] Atmel Inc. *ATmega328P: 8-bit AVR Microcontroller with 32K Bytes In-System Programmable Flash*. URL: https://ww1.microchip.com/downloads/en/DeviceDoc/Atmel-7810-Automotive-Microcontrollers-ATmega328P_Datasheet.pdf.
- [47] Brett Beauregard. *Arduino PID Library - Version 1.2.1*. URL: <https://github.com;br3ttb/Arduino-PID-Library>.
- [48] *Low-Noise, Low-Distortion, INSTRUMENTATION AMPLIFIER, Replacement for SSM2017*. INA217. Datasheet for ANI217 Instrumentation Amplifier. Burr-Brown Products from Texas Instruments. Sept. 2002.
- [49] International Energy Agency. *Solar PV: Technology deep dive*. 2022. URL: <https://www.iea.org/reports/solar-pv>.

Appendix A

Final Arduino Script for the Integrated System

```
1 #include <PID_v1.h>
2
3 int choice; //variable to store the choice(MPPT or PID)
4 int d = 0; //variable to store the duty cycle
5 const int CURRENT_SENSOR_PIN_PV = A1; // ACS712 sensor analog input pin
6 const int VOLTAGE_DIVIDER_PIN_PV = A2; // Voltage divider analog input pin for PV
7 const int VOLTAGE_DIVIDER_PIN_OUTPUT = A0; //Voltage divider analog input pin for the
     ↵ output from the boost converter
8 const int pwmPin = 9; //Output pin to send the PWM signal(Duty Cycle) to the boost
     ↵ converter
9 const int pot = A3; // Analog input pin from the potentiometer to choose the mode of
     ↵ operation
10 int pwmValue; //Variable to store the PWM value
11
12 //Variables for the current sensor
13 float c_sensorValue;
14 const float V_ref = 4.2; //The real value of the 5V of the arduino
15 const float R_shunt = 0.1; //Ohms of the shunt
16 const float R_gain = 68; //Measured value of the gain setting resistor
17 const float Gain = 1 + 10000/R_gain; //InAmp gain
18 float currentError = 1.1473;
19 //const float ACS712_SENSOR_CONSTANT = 0.066; //sensitivity value for the ACS712-30A sensor
20
21 //Variables for PV Voltage divider
22 const float voltageScalar = 5; //Empirically found correction of voltage divider ( $r_2/r_1 +$ 
     ↵ measured fault)
```

Appendix A. Final Arduino Script for the Integrated System

```

23
24 //Variables for MPPT Algorithm
25 const double D_INIT = 0.4;
26 const double D_MAX = 0.9;
27 const double D_MIN = 0.1;
28 const double DELTA_D = 20e-3;
29 double Vold = 0;
30 double Pold = 0;
31 double Dold = D_INIT;
32
33 //Variables for PID Control
34 double setpoint = 24.0;
35 double input, output;
36 double Kp = 0.0135, Ki = 0.09, Kd = 0;
37 //double Kp = 1, Ki = 0, Kd = 0;
38 PID myPID(&input, &output, &setpoint, Kp, Ki, Kd, DIRECT);
39
40 float readCurrent() { //Read the input current from PV
41     c_sensorValue = analogRead(CURRENT_SENSOR_PIN_PV);
42     float current = c_sensorValue*((V_ref)/(1023*R_shunt*Gain))*currentError*1000;
43     return current;
44 }
45
46 double readVoltage() { //Read the input voltage from PV
47     int sensorValue2 = analogRead(VOLTAGE_DIVIDER_PIN_PV);
48     double resistorRatio = (99.9+473)/99.9;
49     double voltage = (((sensorValue2 * 5.0) / 1023.0) * resistorRatio);
50     return voltage;
51 }
52
53 double fcn(double vpv, double ipv) {
54     double D = 0;
55
56     double P = vpv * ipv;
57     double dV = vpv - Vold;
58     double dP = P - Pold;
59
60     if (dP != 0) {
61         if (dP < 0) {
62             if (dV < 0) {
63                 D = Dold - DELTA_D;
64             }
65             else {
66                 D = Dold + DELTA_D;

```

Appendix A. Final Arduino Script for the Integrated System

```

67     }
68 }
69 else {
70     if (dV < 0) {
71         D = Dold + DELTA_D;
72     }
73     else {
74         D = Dold - DELTA_D;
75     }
76 }
77 }
78 else {
79     D = Dold;
80 }
81
82
83 if (D > D_MAX) {
84     D = D_MAX;
85 }
86 else if (D < D_MIN) {
87     D = D_MIN;
88 }
89
90 Dold = D;
91 Vold = vpv;
92 Pold = P;
93
94 return D;
95 }

96
97 void setup() {
98     Serial.begin(9600);
99     pinMode(CURRENT_SENSOR_PIN_PV, INPUT);
100    pinMode(VOLTAGE_DIVIDER_PIN_PV, INPUT);
101    pinMode(pot, INPUT);
102    pinMode(VOLTAGE_DIVIDER_PIN_OUTPUT, INPUT);
103    // Set up PWM output and frequency
104    pinMode(pwmPin, OUTPUT);
105    // Configure Timer1 for Fast PWM mode (mode 14) with no prescaler
106    TCCR1A = (1 << COM1A1) | (1 << WGM11);
107    TCCR1B = (1 << WGM13) | (1 << WGM12) | (1 << CS10);
108    // Set the TOP value to 255 for 8-bit resolution
109    ICR1 = 255;
110    // Configure PID controller

```

Appendix A. Final Arduino Script for the Integrated System

```
111     myPID.SetMode(AUTOMATIC);
112 }
113
114 void loop(){
115     choice = analogRead(pot);
116     if(choice>512){
117         Serial.print("PID Control");
118         Serial.print("\t");
119         d = constantv_mode();
120     }
121     else if(choice<512){
122         Serial.print("MPPT Control");
123         Serial.print("\t");
124         d = mppt_mode();
125     }
126     digitalWrite(pwmPin, d);
127     delay(500);
128 }
129
130 int mppt_mode(){
131     double pvVoltage = readVoltage();
132     float pvCurrent = readCurrent();
133     double dutyCycle = fcn(pvVoltage, pvCurrent);
134     pwmValue = round(dutyCycle * 255);
135
136     //Serial.print(pvVoltage);
137     //Serial.print("\tRaw Current Value: ");
138     //Serial.print(c_sensorValue);
139     //Serial.print("\tCurrent(mA): ");
140     Serial.print(pvCurrent);
141     Serial.print("\t");
142     //Serial.print("\tPOWER(mW): ");
143     //Serial.print(pvCurrent*pvVoltage*1000);
144     //Serial.print("\tDuty Cycle: ");
145     //Serial.print(dutyCycle);
146     //Serial.print("\tPWM Value: ");
147     //Serial.println(pwmValue);
148     int sensorValue = analogRead(VOLTAGE_DIVIDER_PIN_OUTPUT);
149     input = (sensorValue * (5.0 / 1023.0)) * ((19.9 + 2.18) / 2.18);
150     //Serial.print("\tInput Voltage: ");
151     Serial.print(pvVoltage);
152     Serial.print("\t");
153     //Serial.print("\tOutput Voltage: ");
154     Serial.print(input);
```

Appendix A. Final Arduino Script for the Integrated System

```
155     Serial.print("\t");
156     Serial.println(dutyCycle);
157     return pwmValue;
158 }
159
160 int constantv_mode(){
161     int sensorValue = analogRead(VOLTAGE_DIVIDER_PIN_OUTPUT);
162     input = (sensorValue * (5.0 / 1023.0)) * ((19.9 + 2.18) / 2.18);
163     myPID.Compute();
164     if(output>0.9){
165         output = 0.9;
166     }
167     pwmValue = round(output * 255);
168     double pvVoltage = readVoltage();
169     float pvCurrent = readCurrent();
170     Serial.print(pvCurrent);
171     Serial.print("\t");
172     //Serial.print("\tInput Voltage: ");
173     Serial.print(pvVoltage);
174     Serial.print("\t");
175     //Serial.print("\tOutput Voltage: ");
176     Serial.print(input);
177     Serial.print("\t");
178     Serial.println(output);
179     //Serial.print("\tDuty Cycle: ");
180     //Serial.print(output);
181     //Serial.print("\tPWM Value: ");
182     //Serial.println(pwmValue);
183     return pwmValue;
184 }
```

Appendix B

Final MATLAB Script for the MPPT

```
1 function D = fcn(vpv, ipv)
2
3
4
5     D_init = 0.4;
6     D_max = 0.9;
7     D_min = 0.1;
8     deltaD = 20e-3;
9     persistent Vold Pold Dold;
10
11    dataType = "double";
12
13
14    %Assign starting values
15    if isempty(Vold)
16        Vold = 0;
17        Pold = 0;
18        Dold = D_init;
19    end
20
21    P = vpv*ipv;
22    dV = vpv - Vold;
23    dP = P - Pold;
24
25
26    if dP ~= 0
27        if dP < 0
```

```
28     if dV < 0
29         D = Dold - deltaD;
30     else
31         D = Dold + deltaD;
32     end
33     else
34         if dV < 0
35             D = Dold + deltaD;
36         else
37             D = Dold - deltaD;
38         end
39     end
40 else D = Dold
41 end
42
43 if D > D_max
44     D = D_max;
45 elseif D < D_min
46     D = D_min;
47 end
48
49 Dold = D;
50 Vold = vpv;
51 Pold = P;
```